Laboratory measurements of anhydrous minerals mixed with hyperfine hydrated minerals to support interpretation of infrared reflectance observations of planetary surfaces.

Poggiali, G. (1,2)*; Iannini Lelarge, S. (3); Brucato, J.R. (2); Barucci M. A. (1); Masotta, M. (3,4); Corazzi, M.A. (2); Fornaro, T. (2); Brown, A.J. (5); Mandon, L. (6); Randazzo, N. (7)

(1) LESIA-Observatoire de Paris, Université PSL, CNRS, Sorbonne Université, Université de Paris, 5 place Jules Janssen, 92190 Meudon, France.
(2) INAF-Astrophysical Observatory of Arcetri, Firenze, Italy.
(3) Department of Earth Science, University of Pisa, Pisa, Italy.
(4) CISUP, Centro per l'Integrazione della Strumentazione Università di Pisa, Pisa, Italy
(5) Plancius Research, Severna Park, MD 21146, USA
(6) Division of Geological and Planetary Sciences, California Institute of Technology, Pasadena, CA, USA
(7) Earth and Atmospheric Sciences, University of Alberta, Alberta, Canada

*email: giovanni.poggiali@obspm.fr / giovanni.poggiali@inaf.it

Abstract

Identification of water in our Solar System is a key point to understanding the formation and evolution of planetary bodies as well as for astrobiological studies. Scientists identified hydrated minerals as a prime source of H_2O in our Solar System. Minerals such as clays, serpentines and other phyllosilicates were discovered by orbiter and lander spacecraft and ground observations on a large variety of rocky surfaces from Mars to small asteroids using InfraRed (IR) spectroscopy as primary technique. It has already been observed that in the presence of large amounts of hydrated minerals in mixtures with anhydrous minerals, the IR spectra can be dominated by the features of hydrated minerals. However, it is still poorly studied how the IR spectra change in presence of different grain size of the two components. The goal of this study was to investigate the infrared spectroscopic features of anhydrous mineral spectra in presence of low amounts of small grain size hydrated hyperfine particles. We prepared several mixtures using 1 wt% and 5 wt% of very small grain size (< 10 μm) hydrated minerals and 95 wt% and 99 wt% of larger grain size (200-500 μm) anhydrous minerals. We measured the IR reflectance spectrum of these mixtures in the range 8000 - 400 cm^{-1} (1.25 - 25 μm). Results presented here show how the presence of a very limited amount of hydrated minerals with grain size one order of magnitude smaller than the anhydrous component is sufficient to change the IR spectrum, especially in the Near-InfraRed (NIR) region where some of the major hydrated features manifest. On the contrary, the Mid-InfraRed (MIR) part of the spectrum (also identified as thermal infrared) is definitely less affected and

anhydrous mineral features continue to be dominant with slight modifications. This result is of pivotal importance for correctly interpreting the IR reflectance observations of planetary bodies such as Mars or asteroids where a mixing of anhydrous and hydrated minerals can be observed. The presence of strong spectroscopic features due to hydrated minerals can be misinterpreted as a large abundance of this material instead of a spectroscopic effect.

Keywords: infrared spectroscopy, planetary surfaces, hydrated minerals, regolith, remote sensing

1. Introduction

1.1 Scientific context and previous studies

The search for H_2O on rocky planetary surfaces is a key objective of Solar System exploration programs linked with the formation of terrestrial planets and the origin of life on Earth and possibly on other celestial bodies including astrobiological aspects (Domagal-Goldman and Wright 2016). Since the beginning of the spacecraft exploration era, the assessment of water content trapped in mineral matrices has been a primary goal of most planetary space missions. Hydrated minerals may represent one not-negligible source of water on planetary surfaces (Morbidelli et al 2000) and were identified on a wide range of planetary surfaces: from primitive asteroids (Hamilton et al 2019, Kitazato et al 2019) to rocky planets (Mustard et al 2008) and even in Interplanetary Dust Particles IDP (Maurette et al 2020). The investigation of planetary surface composition and the presence of hydrated minerals is based extensively on InfraRed (IR) spectroscopy. Therefore, several mission, both from the ground- and space observatories as well as orbiters, landers and rovers, can benefit of laboratory measurements on mineral mixing. This study is particularly relevant to Mars exploration since infrared spectroscopy instruments have been extensively used for investigating the mineralogy of the surface of Mars, from orbiters like OMEGA (Bibring et al. 2004) and CRISM (Murchie et al. 2007), to rovers such as mini-TES (Christensen et al 2003). OSIRIS-REx and Hayabusa 2 missions studied in detail carbonaceous asteroids finding widespread hydrated materials by infrared spectroscopic observations from NIRS3 (Kitazato et al. 2019) and OVIRS (Hamilton et al 2019, Barucci et al. 2019). Also new asteroid mission like HERA (Michel et al 2022) carrying both an hyperspectral imager ASPECT and a thermal infrared spectrometer TIRI could use these laboratory results to support mineralogical investigations (Skulteti et al 2020). Finally, the planned mission MMX (Kuramoto et al. 2022) to explore the Martian moons will also benefit from this data in the study of the hydrated component possibly present on the surface of Phobos and Deimos.

The analysis of mineral mixtures is a powerful tool for the interpretation of remote sensing data (Horgan et al 2014) and the effect of fine grain size. The latter was extensively studied in the past since <50 μm regolith dominates particle size distributions of many planetary surfaces (a review on this topic is reported in Kiddell et al 2018). The small grain size component can even modify the IR spectrum of subsurface in the case of layer deposition by reducing the spectral contrast of the rock substrate substantially (Johnson et al 2002, Kiddel et al 2018).

Since the beginning of the systematic investigation of the effect of fine particles on IR spectra, several works have been published and their review is outside the scope of this publication. Although several were focused on relatively large particle sizes (20-50 μm or bigger) some focused on smaller particles (<20 μm) but examined only the bulk effects. Pommerol et al (2008) studied in detail the effect of mixture of STx-1 smectite and anthracite, but only one mixture in the work used grain size <25 μm (for both the components) and 5 wt% mixture (but for the dark component). Hyperfine particles were first studied in detail by Mustard & Hays (1997) and Cooper & Mustard (1999) and recently by Brown (2014), Rousseau et al. (2018) and Sultana et al. (2021). All the previous works focused mostly on the effect of hyperfine particles on a single material (either hydrated/anhydrous silicate or others). Only few work examinate the mixture of ahydrous and hydrated minerals: a mixture of hyperfine grains were investigated to match VIRITS observations of comet 67-P with various abundances on three components only (Rousseau et al. 2018), while measurements of olivine and Fe/Mg-clay with different grain size were include in ROMA database in support of Mars exploration (Mandon et al 2020).

In this work, we aim to invesstigate for the first time changes in the IR spectrum of anhydrous minerals following mixing with a hyperfine hydrate component in minute percentages (1 wt% and 5 wt%).

1.2 Hydrated and anhydrous mineral choice rationale

Two hydrated minerals were chosen to be ground at very low grain size: antigorite, a serpentine group mineral, from Złoty Stok (Poland), and montmorillonite, a smecitite group mineral, SAz-1 from Apache county (Arizona, USA).

Antigorite, along with lizardite and chrysotile, is one of the common forms of serpentine with a lamellar appearance and well-defined cleavages. Serpentine group minerals draw the attention of scientists in planetology and astrobiology because they are extremely common in a variety of relevant space environments. Indeed, these minerals are directly linked with the aqueous alteration of rocky surfaces (Moody 1976) and are products of the serpentinization process occurring in hydrothermal vents (Bach et al., 2006, Farkas-Takács et al 2022), which are considered plausible incubators for the first life forms (Shock, E. and Canovas, P. 2010, Braakman, R. 2013). Serpentines were found on Mars (Ehlmann et al., 2009, 2010, 2011;

Brown et al 2010; Viviano-Beck et al., 2014, Changela et al 2022) and they are one of the most abundant components in carbonaceous chondrite meteorites (Cloutis et al 2011) and therefore also present in large amounts on carbonaceous asteroids. Montmorillonite is a hydrous aluminum phyllosilicate of the smectite group formed by precipitation from water solution as microscopic crystals (namely clay minerals). This mineral was first identified on the surface of Mars by rover exploration (Clark III et al 2007) and then found to be very common on the martian surface (Carter et al 2015).

In addition, anhydrous minerals were selected to be representative of a variety of rocky surfaces around the Solar System. We selected two pyroxenes: diopside from St. Lawrence (New York, USA) and enstatite from Norway. We added to the sample set: bytownitic plagioclase, hereafter referred to as bytownite, from Lake View (Oregon, USA); pyrite from Cerro De Pasco (Perù); spinel from Pakistan; and apatite from Morocco. Pyroxenes are probably the most common minerals on rocky surfaces in the inner Solar System. Positive detections were obtained for all the terrestrial planets and some classes of asteroids and meteorites, in particular, they were detected on Mars [Huguenin, 1987; Mustard et al 2005], on basaltic asteroids like V-type [Moskovitz et al. 2008], S-type asteroids [DeMeo et al 2015] and meteorites [Mason, 1968; Dodd, 1981; Rubin and Ma 2021]. Plagioclase, a feldspar group mineral, is also typically present in basaltic lithologies, being very common on terrestrial planets and rocky bodies in the inner Solar System: it was found to be the most abundant component of the Moon highlands (Ohtake et al 2009), and it was also observed on Mars (Milam et al 2010). Pyrite is an iron sulfide found in martian meteorites (Agee et al., 2013) and is suspected to be involved in the formation of the sulfate-rich regions on Mars (Zolotov and Shock, 2005). In general, iron sulfide minerals (i.e. pyrrhotite) are a very common materials in asteroid composition (Gaffey 1986, Scott 2020). The last two anhydrous minerals, spinel and apatite, respectively oxides and phosphates, were observed in several geological settings around the Solar System (Haggerty, 2016). Fe–Cr–Ti spinel was detected in a martian meteorite (Yu and Gee, 2005), whereas apatite is ubiquitous in extraterrestrial materials and was detected so far in several martian meteorites (e.g. Hu et al., 2014, McCubbin et al., 2016). Some of the minerals used in this work were already measured and analyzed in previous work carried on in Arcetri Laboratory showing similar infrared spectrum and additional analysis (Fornaro et al 2018, Poggiali et al 2021, Poggiali et al 2022).

2. Methods

2.1 Preparation of sample mixtures

All the minerals were grounded in a Retsch Planetary Ball Mill PM100 (agate jar and spheres) and sieved using Retsch Vibratory Sieve Shaker AS200. Anhydrous minerals were selected

in grain size 200-500 μm and washed with an ultrasonic bath to remove the possible amount of smaller grains that remained. Hydrated minerals antigorite and montmorillonite were sieved mechanically to size < 20 μm using the smallest possible Retsch woven wire mesh sieve. In a second step, the powder obtained with mechanical sieving was further sieved in grain size < 10 μm using a technique based on the time of fall deposition in water. We suspended the mineral particles in a tall graduated cylinder filled with ultra-pure water and we evaluated the time of fall for each mineral based on its density to have grains with a diameter more than 10 μm below a certain level of the cylinder after a fixed time. Then we removed the suspension above that level using a pipette and centrifuged it to separate the mineral pellet, which we dried in an oven at 50 °C. The procedure was repeated several times to have a suitable amount of fine grain material to be used for preparing the mixtures.

For each anhydrous mineral, a series of mixtures were prepared by adding 1 and 5 wt% of each hydrated mineral. After some preliminary tests, we developed the following mixing protocol:

1. hydrated and anhydrous minerals were weighted in proper amounts to prepare mixtures and placed in the same eppendorf tube, a small 2.0 mL disposable test tubes;
2. 1 mL of ethanol was added to the minerals and the eppendorf tube was placed for 10 seconds in an ultrasonic bath to energize the suspension and enhance the mixing between the two components;
3. the suspension of minerals and ethanol was dried in an oven at a temperature of 45° C for one week to remove the solvent and reduce the amount of ambient water adsorbed on the mineral grains.

Having attempted several methods of mix preparation including spiking and deposition from a suspension of ethanol and small grains, we believe this is the best choice in terms of time-effectiveness and end product. During the measurements, all the samples were stored in the oven and taken only for the time necessary for acquiring the IR spectrum (in vacuum conditions). We prepared 7 mixtures of hydrated-anhydrous minerals listed in Table 1.

mineral (big grain size)	mix with antigorite	mix with montmorillonite
diopside	1 wt% and 5 wt%	1 wt% and 5 wt%
enstatite	1 wt% and 5 wt%	1 wt% and 5 wt%
bytownite	1 wt% and 5 wt%	1 wt% and 5 wt%
pyrite	1 wt% and 5 wt%	1 wt% and 5 wt%
apatite*	1 wt%	-
spinel*	1 wt%	-

Table 1 Samples prepared for the IR analysis of anhydrous-hydrated minerals mixtures. *Apatite and spinel were mixed only with antigorite and only at 1 wt% concentration due to a shortage of material.

2.2 FTIR analysis

All infrared measurements were performed at the INAF-Astrophysical Observatory of Arcetri in Florence, Italy. Fourier Transform InfraRed (FTIR) reflectance spectra were collected using a Bruker VERTEX 70v interferometer interfaced with Harrick Praying Mantis™ for Diffuse reflectance infrared fourier transform spectroscopy (DRIFTS) analysis in biconical off axis geometry. Such an experimental set-up has some advantages: very high collection efficiency, and accurate determination of the reflectance profile by measuring diffuse reflectance at 90° with respect to the principal plane. MIR Globar source, DTGS detector, and optical elements in KBr allow for collecting spectra on a wavenumber range between 8000 and 400 cm^{-1} (1.25–25 μm in wavelength). Spectral resolution during acquisition was 4 cm^{-1} and each spectrum was the result of 100 scans. Infragold® stardard from Labsphere was used to acquire the reference background.

The sample taken from the storage oven was placed in a removable sample holder of the Praying Mantis maintaining a 50°C temperature during the transfer (by placing the sample holder on a heating plate) in order to reduce possible adsorption of atmospheric water. Once the sample was placed in the Praying Mantis, the sample chamber was evacuated with a turbomolecular pump with a minimum pressure attainable of $5 \cdot 10^{-5}$ mbar. The sample was left in vacuum condition for 30 min prior the measurements to enhance the removal of adsorbed water.

Analysis of the spectroscopic features was carried on independently **in the two separated ranges** covered by our measurments. In the NIR range we started with the automatic identification of peak positions, obtained with a Matlab routine, followed by an in depth visual inspection. In the MIR range we carried on a visual analysis of the most important spectroscopic features present in the wavelength range.

2.3 SEM analysis

Scanning Electron Microscopy (SEM) analyses were carried out using the field emission scanning electron microscope (FE-SEM) FEI Quanta 450 ESEM FEG, equipped with an energy-dispersive microanalytic system (EDS) Bruker's QUANTAX EBSD/EDS at the Centro per l'Integrazione della Strumentazione dell'Università di Pisa (CISUP). Backscattered electrons (BSE) and secondary electrons (SE) images of the small grain size samples were acquired at different magnifications to determine the grain size distribution and composition using image analysis techniques.

3. Results

3.1 Textural and chemical features

SEM images of mineral grains and mixtures are reported in Figure 1. Visual inspection already reveals that the sieving process was efficient to select the grain size both for the hyperfine hydrated component and the anhydrous component. SEM image analysis allowed us to measure the average grain size for each batch of minerals (minimum, maximum and average dimensions determined by image analysis of backscattered electron images, are reported in Table 2). Since grains are not regular (in particular for the bigger size 200-500 μm anhydrous mineral samples) we reported two values, the minor and major axis of the approximated ellipse, instead for the hyperfine component grains are approximated as circles and only the diameter is reported (in the column of the major axis in Table 2).

The sieving process for hydrated minerals produced homogenous samples with a slightly different average diameter: 1.47 μm for serpentine and 3.58 μm for montmorillonite and a shifted grain size distribution as visible in Supplementary Material Figure S2. Differences between the two samples can be linked to the grinding and/or sieving process as well as the natural properties of the mineral, in our work the goal was to compare hyperfine hydrated minerals with bigger dimension anhydrous minerals and, being both serpentine and montmorillonite samples characterized by a grain size < 10 μm, we proceeded with our analysis leaving the study of grain size distribution differences to future works. On the other side, the anhydrous mineral sieving process and cleaning produced a sample set in the planned range as visible in Table 2 where we report minimum, maximum, and average dimensions for minor and major axes of the ellipse enclosing the single grain. Both the average minor and major axes for each mineral are in the range selected (200-500 μm) except for enstatite with an average major axis of around 870 μm. This excess in one of the dimensions of the sample can be related to the orthorhombic crystal system of enstatite resulting in grains with an elongated shape that is clearly visible in Figure 1, panel D.

The mixing process of the hydrated and anhydrous minerals was also checked with SEM confirming the deposition of hyperfine grains on the surface of the bigger anhydrous grain as visible in Supplementary Material Figure S3 (see also Supplementary Material Figure S4 for a detailed example of before and after the mixing procedures). The chemical composition of the mineral grains obtained by SEM-EDS is reported in Table S1.

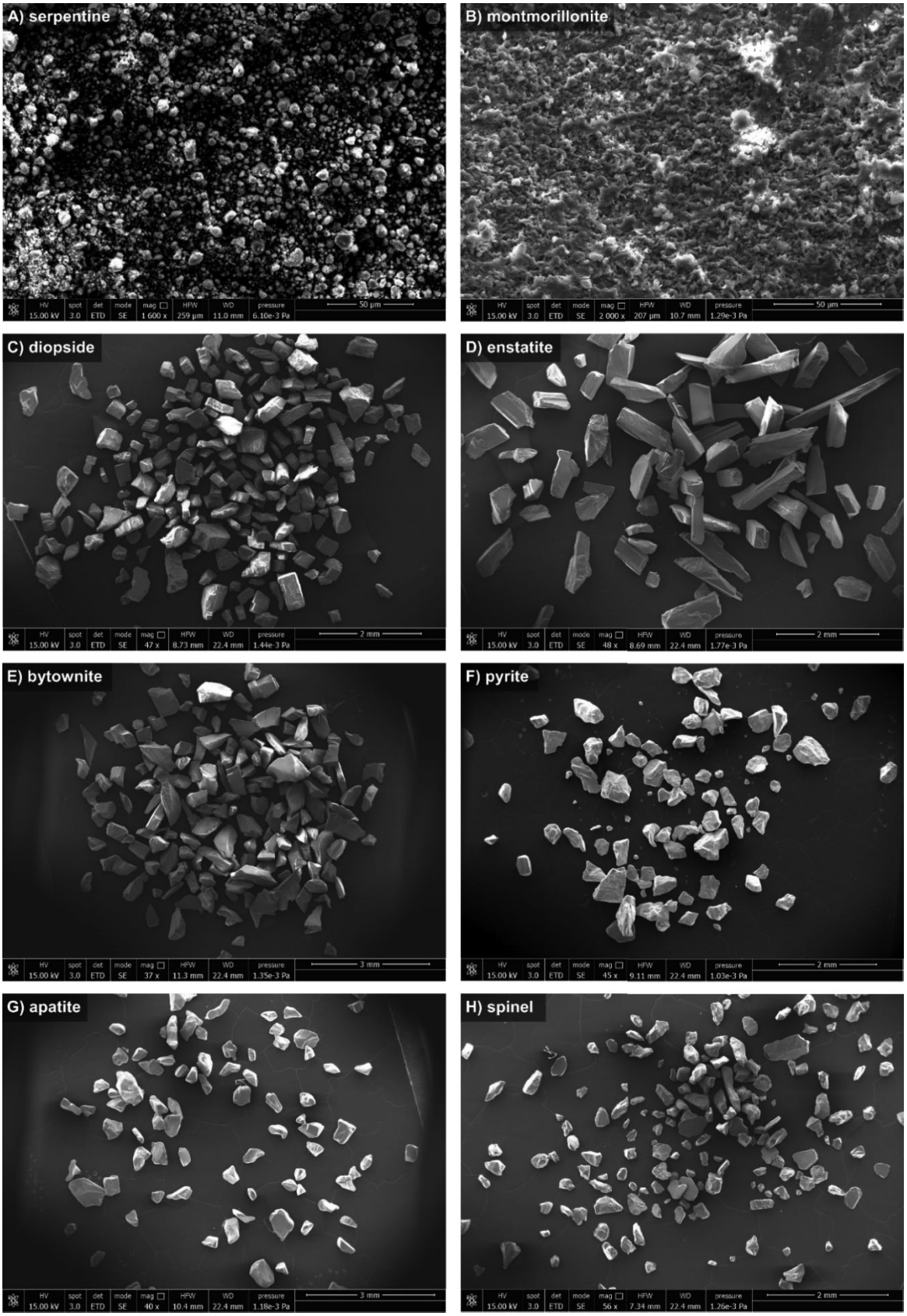

Figure 1 Secondary electrons SEM images of the mineral samples used to produce the mix. **Image order**: (A) serpentine, (B) montmorillonite, (C) diopside, (D) enstatite, (E) bytownite, (F) pyrite, (G) apatite and (H) spinel. **The scalebar at the bottom left of each pictures** varies from 50 µm (for

hyperfine minerals) to 2/3 mm for anhydrous minerals, the precise scale value is reported in each panel bottom right corner.

minerals	N. of grains	minor axis [µm]			major axis or diameter [µm]		
		min / max	avg	σ	min / max	avg	σ
serpentine	2477	-	-	1.24	0.10 / 9.96	1.47	1.24
montmorillonite	967	-	-	1.68	0.57 / 11.7	3.58	1.68
diopside	183	8 / 562	244	89	174 / 961	401	150
enstatite	65	180 / 560	373	117	276 / 2548	869	407
bytownite	142	151 / 660	315	103	225 / 1125	573	205
pyrite	94	54 / 571	257	127	101 / 863	401	202
apatite	78	106 / 611	274	88	218 / 936	464	136
spinel	161	62 / 386	170	65	102 / 829	273	114

Table 2 Minimum, maximum, average grain size and standard deviation in mineral samples from SEM image analysis. As visible in Figure 1 panels A and B, hyperfine serpentine and montmorillonite grains show a quasi-circular shape so we evaluate only the diameter (reported as the major axis in the table).

3.2 Infrared spectroscopy

3.2.1 General consideration

All the acquired spectra of hydrated-anhydrous mixtures are shown in Figure 2 - 6. In all the plots of IR spectra, the X-axis on the bottom shows linearly the wavenumber of the infrared spectrum while the corresponding wavelengths are shown on the top X-axis. For each plot, the solid line represents the IR spectrum of the base component with grain size 200-500 µm. Dotted and dash-dot lines represent mixtures with 1 wt% and 5 wt% of hydrated minerals with < 10 µm grain size, respectively.

Most silicate minerals present distinct bands in the MIR range often referred to as reststrahlen bands and linked with Si-O vibration in the mineral lattice. In general, we can see that between 1200 and 850 cm^{-1} (about 8 and 12.0 µm) there are bands due to the asymmetric stretching mode of the Si-O bond. Bands due to symmetric stretching of Si-O-Si, or Al-O-Al, or a combination of the two, show up in the region 850-600 cm^{-1} (12-16.5 µm), while bands due to Si-O-Si bending and other deformation modes appear below 600 cm^{-1} up to our limit of acquisition at 400 cm^{-1} (25 µm) (Salisbury et al 1989). The MIR range is characterized also by two other important features: Christiansen features and **Transparency features**. The former is linked with mineralogy of the samples and it's produced by a rapid changes in the refractive index that, approaching the refractive index of the surrounding medium, results in minimal

scattering (Conel 1969). The latter, is due to volume scattering from particles with small grain size (tens of μm, usually < 50 μm) (Salisbury et al 1991).

Although some of the minerals chosen for the mixtures are listed in manuals as anhydrous, a prominent 3600 cm^{-1} (2.7 μm) hydrated band [from now HydB] appears in the IR spectrum. Literature studies showed that H_2O can be stored in nominally anhydrous minerals (NAMs) as hydrogen structurally bound to specific oxygen sites (Yang et al 2012) and water may be present in fluid inclusions, as interlayer H_2O in sheet silicates, as water of hydration showing strong infrared features (Salisbury and Walter 1989) and also as adsorbed atmospheric water on the surface not removed with mild heating. In case of a strong OH/H_2O contamination also minor bands in the NIR region can appear at about 7150 and 5550 cm^{-1} (1.4 and 1.8 μm) likely associated with the overtone of the 2.7 μm band and the H_2O combination band, respectively (Clark et al. 1990). However, the HydB that may be present in anhydrous minerals is generally different from that of hydrated minerals (see for example the case of enstatite in this study) and can be easily distinguished. Moreover, the presence of hydrated minerals is generally able to drastically change the HydB with respect to the pure starting mineral, whether this is totally anhydrous or NAM. Working with natural minerals in which a HydB may already be present also in anhydrous minerals makes difficult a precise quantification of the spectroscopic feature in terms of depth and band area.

A second general consideration can be made on the **Transparency features**. This infrared band is usually well visible in the spectra of samples with grain size less than 50 μm around 1200-800 cm^{-1} (8-12 μm) depending on the composition (Salisbury et al 1991). In the spectra of our mixture at 1 wt% Figure 2 – 6 the band is not clearly visible while is probably inducing some modification in the spectra of mixture at 5 wt%. Being the features related to volume scattering of a sample of small grains, its lack in our mixtures with 1 wt% can be linked to the observed dispersed position of hyperfine grains on the surface of the big ones (Supplementary Material Figure S3).

The detailed IR results of the various samples are presented below on a case-by-case basis for the individual anhydrous minerals in the mixtures.

3.2.1 Diopside

Base mineral features

The spectrum of pure diopside is shown as a solid line in Figure 2. The NIR range is characterized by several minor bands linked probably with OH-defects in pure natural diopside 7354, 7182, 5207, 4362, 4320, and 4189 cm^{-1} (1.36, 1.39, 1.92, 2.29, and 2.38 μm), also intersecting the shallow pyroxene band centered around 4400 cm^{-1} (2.25 μm), typical of iron-rich calcic pyroxene. At a shorter wavenumber (longer wavelength) the spectrum shows a complex HydB: a sharp peak appears at 3674 cm^{-1} (2.72 μm) linked with the presence of OH-

defects while secondary broad bands are visible nearby 3600 cm^{-1} (2,77 μm) and 3450 cm^{-1} (2.89 μm) due to H_2O/OH presence.

Moving to the MIR spectrum we observe a complex series of overlapping bands in the "cross-over" region between 2200 cm^{-1} and 1200 cm^{-1} (4.5-8.3 μm). Bands in the "cross-over" region are due to overtone-combinations of strong molecular and crystal lattice vibrations at longer wavelengths known as reststrahlen bands (Bowey & Hofmeister, 2005). Some well-defined reststrahlen bands peaked at about 1115, 1015, 962 and 920 cm^{-1} (8.97, 9.85, 10.39 and 10.87 μm) due to Si-O asymmetric stretching with an additional shoulder around 865 cm^{-1} (11.56 μm). O-Si-O symmetric stretching is responsible for the small peak at 671 and 635 cm^{-1} (14.90 and 1575 μm). At the limit of our range of acquisition, we found several peaks due to chain deformation and Si-O-Si bending at 556, 511, and 482 cm^{-1} (17.98, 19.56, and 20.75 μm) with several shoulder features in all this region (Omori 1971).

Diopside mixed with serpentine

The addition of a small amount of serpentine with a grain size <10 μm to pure diopside with grain size 200-500 μm causes some spectroscopic changes as shown in the top panel of Figure 2. In the NIR region, although the spectral contrast is decreased, the OH-defects diopside bands are still detectable and minor bands of diopside are overlapping OH/H_2O serpentine bands at 7395, 7145, 5200, and 4302 cm^{-1} (1.35, 1.40, 1.92, and 2.32 μm) with no strong modifications. The HydB is strongly modified after mixing with serpentine and even the 1 wt% of the small grain hydrated mineral is able to change the shape of the band as shown in Figure 7A. The addition of 5 wt% serpentine to diopside changed drastically the region of HydB with the resulting spectrum showing a band very close to the HydB of pure serpentine (as shown in Supplementary Material Figure S1, top panel).

Moving to the MIR region, the "cross-over" bands between 2200 cm^{-1} (4.5 μm) and 1200 cm^{-1} (8.3 μm) are slightly modified by the mixing with hydrated minerals, mainly through a decrease in the intensity of the bands which, however, do not change neither position nor shape. In the reststrahlen bands region, while maintaining the general appearance of the diopside spectrum, some changes are observed. The peak at 1115 cm^{-1} (8.97 μm) increases its intensity with the addition of 1 wt% serpentine and then decreases when using 5 wt% hydrated minerals; in both cases, the band tends to become thinner. The peaks at 1015, 962 cm^{-1} and 920 cm^{-1} (9.85, 10.39, and 10.87 μm) are slightly modified by the addition of 1 wt% serpentine (mainly in intensity for all and the shape only of 1015 cm^{-1} band) while at 5 wt% serpentine we notice a change in relative height with the peak at 920 cm^{-1} becoming significantly more intense and changing the shape possibly due to the appearance of the **Transparency feature** of serpentine. Although intensity seems to vary not linearly along the spectrum for 1 wt% mixture, it decreases everywhere for the 5 wt% mixture. In the last region of our spectrum, the shape

and peaks do not seem to change strongly except for the peak at 556 cm^{-1} (17.98 μm) which decreases in relative intensity compared to the others in the 1 wt% mix.

Diopside mixed with montmorillonite

When montmorillonite is added to the diopside instead of serpentine (Figure 2, bottom panel) less intense changes are observed compared to the mixtures with serpentine mostly related to the decrease in intensity. The mixture of diopside with 1 wt% of montmorillonite does not show visible changes in band shape or position. The HydB does not change its shape compared to the pure diopside and also the MIR region, although affected in intensity, maintains the original shape of the reststrahlen bands. Considering the mixtures with 5 wt% of montmorillonite, the changes in the diopside spectrum become more pronounced although still barely visible. In the NIR range, some minor features appear around 7415, 4730, 4090, 4060, and 3901 cm^{-1} (1.35, 2.11, 2.44, 2.46, and 2.56 μm) probably linked with some of the minor features in the phyllosilicate spectrum (see black arrows in Supplementary Material Figure S1, bottom left panel). At the same time, the minor features already visible in the diopside spectrum (and likely attributable to OH-defects) become more intense. The diopside HydB (Figure 7E) changes accordingly with the montmorillonite HydB but the diopside band shape remains well recognizable.

In the MIR region we noticed some modification in bands around 1090, 920 and 460 cm^{-1} (9.17, 10.86, and 21.74 μm) with the appearance of new small peaks at 757, 686, and 540 cm^{-1} (13.21, 14,58 and 18.51 μm) the former linked probably with **Transparency feature** due to hyperfine grains, while the latters associated **surprisingly** with very small features in the pure montmorillonite spectrum (Supplementary Material Figure S1, bottom right panel).

3.2.2 Enstatite

Base mineral features

The enstatite spectrum (solid line in Figure 3) in our acquisition range in the NIR shows the well-known big absorption band at about 5400 cm^{-1} (around 2 μm) due to Fe^{2+} in M2 crystallographic site that characterizes pyroxene minerals. A complex band is visible around 3750-3300 cm^{-1} (2.6-3 μm) with two main peaks at 3514 and 3417 cm^{-1} (2.85 and 2.93 μm) and several shoulders (3700, 3650, 3590, 3550 cm^{-1} or 2.70, 2.74, 2.78, 2.82 μm). These bands are due to natural OH-defects in pure enstatite.

Between 2200 and 1500 cm^{-1} (4.5-6 μm) we observe the “cross-over” region characterized by several bands with a poor contrast compared to the continuum. The reststrahlen region shows the characteristic band of enstatite and Mg-rich pyroxene with major peaks at 1065, 980, and 868 cm^{-1} (9.39, 10.20 and 11.52 μm) due to Si-O asymmetric stretching, and peaks at 548, 515 and 452 cm^{-1} (18.24, 19.42 and 22.12 μm) due to O-Si-O bending and bond deformation

(Bowey et al 2020). Both the series of bands present several minor peaks and shoulders. In between the two main groups of bands, we find two well-defined peaks, although with a smaller intensity, at 691 and 650 cm^{-1} (14.47 and 15.38 μm) possibly linked with Si-O-Si symmetric stretching.

Enstatite mixed with serpentine

Adding serpentine in grain size <10 μm (Figure 3, bottom panel), we observe several changes along the spectrum as reported in Figure 3, top panel. The pyroxene 2 μm band contrast is affected more when enstatite is mixed with 5 wt% serpentine while the contrast decreases slightly by adding only 1 wt% of the hydrated mineral. Several faint adsorption features appear next to the broad band, in particular at 7354, 7186 and 4298 cm^{-1} (1.40, 1.39, and 2.32 μm) linked with OH vibration overtones and Mg-/Fe-bearing phyllosilicate (Carter et al 1990) (and indeed visible in the pure serpentine spectrum in Supplementary Material Figure S1, bottom left panel). The structure of HydB is modified drastically (see a normalized detail of HydB in Figure 7B) and the OH peak of serpentine at 3666 cm^{-1} (2.72 μm) becomes the most intense feature with an intensity of 20% higher with respect to the OH-defect peak of enstatite of the mixture spectrum (and almost 30% higher compared to the OH-defect peak of pure enstatite spectrum). It is important to note that in the pure spectrum of enstatite there was no peak at 3666 cm^{-1}. As for the other mixtures, 5 wt% of serpentine can show a feature of HydB very close to the one of the pure phyllosilicate.

The "cross-over" region (2200 and 1500 cm^{-1} or 4.5-6 μm) is only slightly modified by the presence of the mineral hydrate, especially in the relative intensity of the bands. Coming to the reststrahlen band region we observe an overall modification of the minor peaks although the main bands remain mostly linked with enstatite, in particular, peaks at 1133 and 1065 cm^{-1} (8.82 and 9.39 μm) change the relative intensities: they invert in the 1 wt% mixture (peak at 1133 cm^{-1} more intense than the peak at 1065 cm^{-1}) and become comparable in 5 wt% mixture. The peak at 980 cm^{-1} (10.20 μm) becomes comparable with the nearby peaks while the O-Si-O band and peaks between 600 and 400 cm^{-1} change in intensity in proportion to the percentage of hydrated mineral but slightly in relative intensities. A peak at 721 cm^{-1} (13.87 μm) increases its intensity in the 1 wt% mixture but returns barely visible in the 5 wt% mixture. As for montmorillonite mixed with diopside, this feature seems not directly related to a prominent feature in the serpentine spectrum.

Enstatite mixed with montmorillonite

Adding small-grained montmorillonite (Figure 3, bottom panel) to enstatite we observe some changes: intensity increases when the percentage of the mix is 5 wt% for montmorillonite and remains comparable (or decreases slightly) for 1 wt% mixture. Pyroxene band at about 5500 cm^{-1} (1.8 μm) is slightly affected by the presence of montmorillonite, with moderate changes

only with 5 wt% of phyllosilicate in the mixture. HydB is almost unmodified in the mixture of 1 wt% montmorillonite with enstatite (Figure 7F) while in the 5 wt% mixture an additional peak appears at 3610 cm^{-1} (2.77 μm) due to the presence of the phyllosilicate, although its intensity is lower than enstatite OH-defects peaks intensity.

In the MIR range, while the "cross-over" region is only affected in slope, the reststrahlen band region shows moderate modifications. In the 1 wt% mixture we observe a general decrease of intensity and also some modification of relative intensity between the peak at 1133 cm^{-1} and 1065 cm^{-1} (8.82 and 9.39 μm, due to Si-O stretching) comparable to the effect of the mixture of enstatite and serpentine. At 901 cm^{-1} (11.10 μm) a more prominent shoulder appears in the spectra of the 1 wt% and 5 wt% mixture linked probably with the broad shoulder observed in the pure montmorillonite spectrum (Supplementary Material Figure S2, bottom right panel). The peak at 650 cm^{-1} (15.38 μm) in pure enstatite and 1 wt% mixture spectrum shifts toward 644 cm^{-1} (15.53 μm) in the 5 wt% mixture spectrum, once again, this peak is not directly linked with montmorillonite spectrum features. The region at 600-500 cm^{-1} (16-20 μm) is affected mostly in intensity with a decrease of original intensity with the 1 wt% mixture and an increase in intensity for the 5 wt% mixture.

3.2.3 Bytownite

Base mineral features

The spectrum of bytownite (solid line, Figure 4) is very featureless in the NIR range: at the limit of acquisition, we observe the broad and shallow Fe^{2+} band near 8000 cm^{-1} (1.25 μm) (Adams & Goullaud, 1978). A faint HydB is present at 3626 cm^{-1} (2.76 μm) related to OH/H_2O defect in the plagioclase mineral but with an intensity of about 2% with respect to the continuum. No other minor bands due to OH-defect were observed in the spectrum although several times HydB and other related bands are present in spectra shown in the literature (see for example the bytownite spectrum in USGS library id:HS105.4014).

Moving to the MIR region we note a very featureless "cross-over" region. The reststrahlen bands region is characterized by a series of peaks due to different vibration modes: Si-O asymmetric stretching at 1149 cm^{-1} (8.70 μm), with a shoulder at 1192 cm^{-1} (8.38 μm), and a double peak at 1000 and 950 cm^{-1} (10 and 10.52 μm). A broad peak at about 750 cm^{-1} (13.3 μm) is linked with symmetric stretching of Si-O while a series of the peak at 628, 608, 573 cm^{-1} (15.92, 16.45, 17.45 μm) is due to Si-O-Si bending. This mode produces a peak at 542 cm^{-1} (18.45 μm) when coupled to M-O stretching (Iiishi et al 1971a and 1971b). The last peak visible in our spectrum at 465 cm^{-1} (21.50 μm) is due to bending and deformation.

Bytownite mixed with serpentine

The addition of serpentine with grain size < 10 μm in a mixture with bytownite at 1 wt% and 5 wt% (dotted and dash-dotted line, respectively, in Figure 4, top panel) induces several changes in the resultant spectrum. In the NIR region, two bands of serpentine appear at 7340/7180 cm^{-1} (1.36/1.39 μm) and 4301 cm^{-1} (2.3 μm) linked with OH/H_2O overtone and OH-Mg-OH translation combined with OH stretching, respectively (Wu et al 2021). These bands are very faint in the 1 wt% mixture, in particular the Mg-OH band, but more accentuated in the 5 wt% mixture, where the Fe^{2+} bytownite band at 8000 cm^{-1} (1.25 μm) is also affected. HydB was almost absent in the bytownite spectrum and mixing with serpentine led to the appearance of a deep band of hydrates peaking at 3668 cm^{-1} (2.72 μm) which were totally analogous to that of pure serpentine (detail of HydB in Figure 7C and pure serpentine spectrum visible in Supplementary Material Figure S1).

The "cross-over" region (2200-1200 cm^{-1} or 4.5-8.3 μm) is partially affected by the presence of silicate hydrate. No well-defined bands are present in this region of the bytownite spectrum, and the major change other than continuous is focused around 1600 cm^{-1} (6.25 μm) where there is an intense serpentine band due to the presence of H_2O/OH (clearly visible in Supplementary Material Figure S1, bottom left panel). Contrary to the "cross-over" region the reststrahlen band region shows a major contribution from the phyllosilicate spectrum. The peak at 1149 cm^{-1} (8.70 μm) is slightly modified towards a more symmetric peak while the double peak at 1000 and 950 cm^{-1} (10 and 10.52 μm) changes drastically with a single peak at 925 cm^{-1} (10.81 μm) and a small broad shoulder replacing the 1000 cm^{-1} (10 μm) peak. These could be related to the appearance of the **Transparency feature** due to the hyperfine serpentine grains. We noticed a decreasing spectral contrast for the peak at 750 cm^{-1} (13.3 μm) and a deformation in the final series of peaks at 628, 608, 573 cm^{-1} (15.92, 16.45, 17.45 μm) with a change in relative intensities and a shift of the second and third peak at 592 and 575 cm^{-1} (16.89 and 17.39 μm). In this range, only the peak at 542 cm^{-1} (18.45 μm) is still present although with reduced intensity.

Bytownite mixed with montmorillonite

Using montmorillonite with grain size < 10 μm in the mixture instead of serpentine, again at 1 wt% and 5 wt% percentage with bytownite (dotted and dash-dotted line, respectively, in Figure 4, bottom panel), modifications appear along the spectrum of bytownite even if with lower intensity compared to serpentine. The shallow Fe^{2+} band near 8000 cm^{-1} (1.25 μm) is only partially affected by the presence of a band at 7260 cm^{-1} (1.38 μm), while two faint bands appear at 5263 cm^{-1} (1.90 μm) and 4516 cm^{-1} (2.21 μm). All these bands are linked with OH/H_2O overtones and Mg-O/Fe-O vibrations in montmorillonite. As for the serpentine mix,

the HydB appears stronger than the bytownite band which it is reasonably related to OH defects or not optimal removal of adsorbed water on the mineral (Figure 7G).

Once again, the "cross-over" region is slightly affected with a hint of modification around 1600 cm^{-1} (6.25 µm), and moving to the reststrahlen band range between 1149 and 950 cm^{-1} (8.70-10.53 µm) also these peaks appear to be comparable with the spectrum of sole bytownite with some small modification in relative intensities and shoulder strength. The band at 750 cm^{-1} (13.33 µm) gradually changes as the percentage of montmorillonite increases with the appearance of a shoulder at 730 cm^{-1} (13.70 µm) in the 1 wt% mix, becoming the most prominent peak in the 5 wt% mix. In contrast to the adjacent region, the bands between 650 and 500 cm^{-1} (16.6-20 µm) are definitely affected by the presence of montmorillonite with an extreme change in relative intensities. Once again, the peak at 542 cm^{-1} (18.45 µm) seems to be affected by the presence of montmorillonite.

3.2.4 Pyrite

Base mineral features

Compared with other minerals in our sample set, pyrite has a featureless appearance. We note a faint broad band centered around 6100 cm^{-1} (1.64 µm) and a decrease in intensity towards the end of the acquisition range at 500/400 cm^{-1} (20/25 µm). The spectrum acquired for this work is in agreement with the reference diffuse reflectance spectrum from National Institute of Standard and Technology NIST quantitative infrared database (Chu et al 1999).

Pyrite mixed with serpentine and montmorillonite

Additions of serpentine at 1 wt% and 5 wt% (Figure 5, top panel) induce the appearance of H_2O/OH overtone and Mg-OH bands respectively at 7300 cm^{-1} (1.37 µm) and 4295 cm-1 (2.33 µm) while montmorillonite mix at the same percentage does not show minor bands in this region (Figure 5, bottom panel). The HydB is differently affected by the mixing with the two phyllosilicates: being almost negligible in pure pyrite it appears with a higher intensity and a clear shape in both the mixtures of serpentine (1 wt% and 5 wt%), while it is present faintly in the mixture at 5 wt% of montmorillonite and only hinted in the mix at 1 wt% as observable in Figure 7D and 7H.

In the MIR region, the mixture of pyrite and montmorillonite again shows very faint modification from the pure pyrite spectrum, while the mix with serpentine (both at 1 wt% and 5 wt%) shows some features not all comparable with the pure serpentine spectrum. In particular, the broad absorption feature around 1000 cm^{-1} (10 µm) is reversed in the spectrum of pure serpentine (Supplementary Material Figure S1, bottom right panel), as well as the feature around 600 cm^{-1} (16.66 µm).

3.2.5 Spinel and apatite

Base mineral features and change due to mixing

We also prepared the other two mixtures using spinel and apatite and only serpentine at 1 wt% (due to a shortage of material). The two minerals spectra are not significantly affected by the addition of serpentine probably due to the large abundance of features across the spectrum and the presence of complex OH related bands in the region between 4000 and 3000 cm^{-1} (2.50-3.33 μm).

In the NIR region, the spinel spectrum is slightly changed by the mixture with serpentine with small changes in spectral slope (Figure 6, bottom panel). Moreover, the spinel spectrum dominates the entire wavelength range analyzed with a small modification in the double peak OH related band with the first peak at 3695 cm^{-1} (2.71 μm) becoming more intense than the second at 3658 cm^{-1} (3.66 μm). Minor modifications in intensity are also visible around 1965 cm^{-1} (i.e. 5 μm) and 700 cm^{-1} (i.e. 14 μm) with the spectrum of the serpentine-spinel mixture slightly more intense than the spectrum of the pure joint.

The spectrum of apatite is reduced in intensity in the NIR region and all the bands are reduced in contrast but no new bands appear related to the phyllosilicate (Figure 6, top panel). A small change is observed in the HydB where the appearance of a small peak at 3668 cm^{-1} (2.72 μm) due to the serpentine affects also the nearby band at 3762 cm^{-1} (2.66 μm) making it a shoulder of the new feature. The rest of the spectrum continues to have a lower intensity than the pure apatite spectrum but no other changes in the bands are observed.

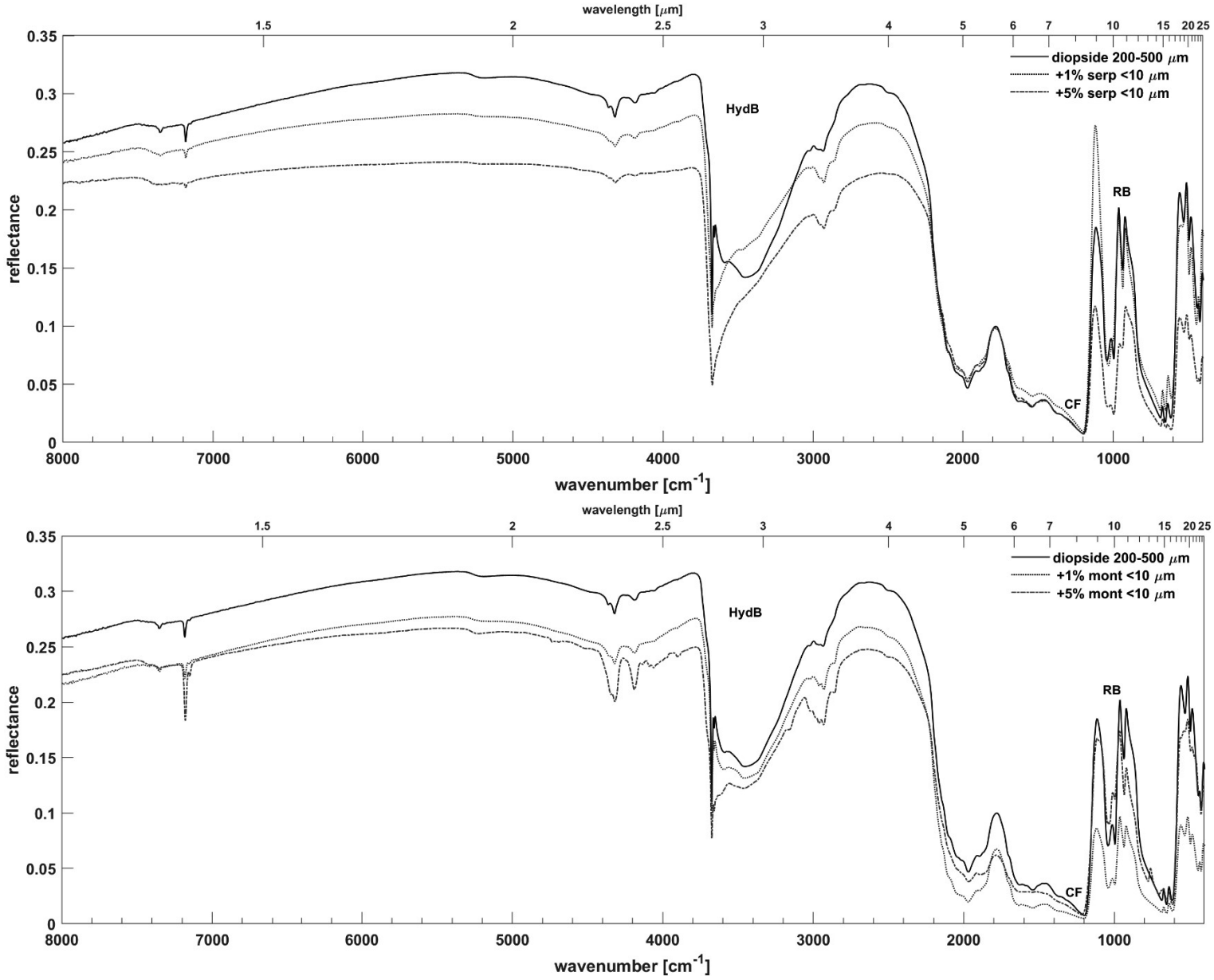

Figure 2 FTIR reflectance spectrum for diopside with grain size 200-500 µm (solid line) compared to mixtures with serpentine (top) and montmorillonite (bottom) with < 10 µm grain size, at 1 wt % concentration (dotted blue line) and 5 wt% concentration (dash-dot red line). Position of the hydrated band (HydB), the Christiansen feature (CF) and the reststrahlen bands (RB) are highlighted on the spectrum.

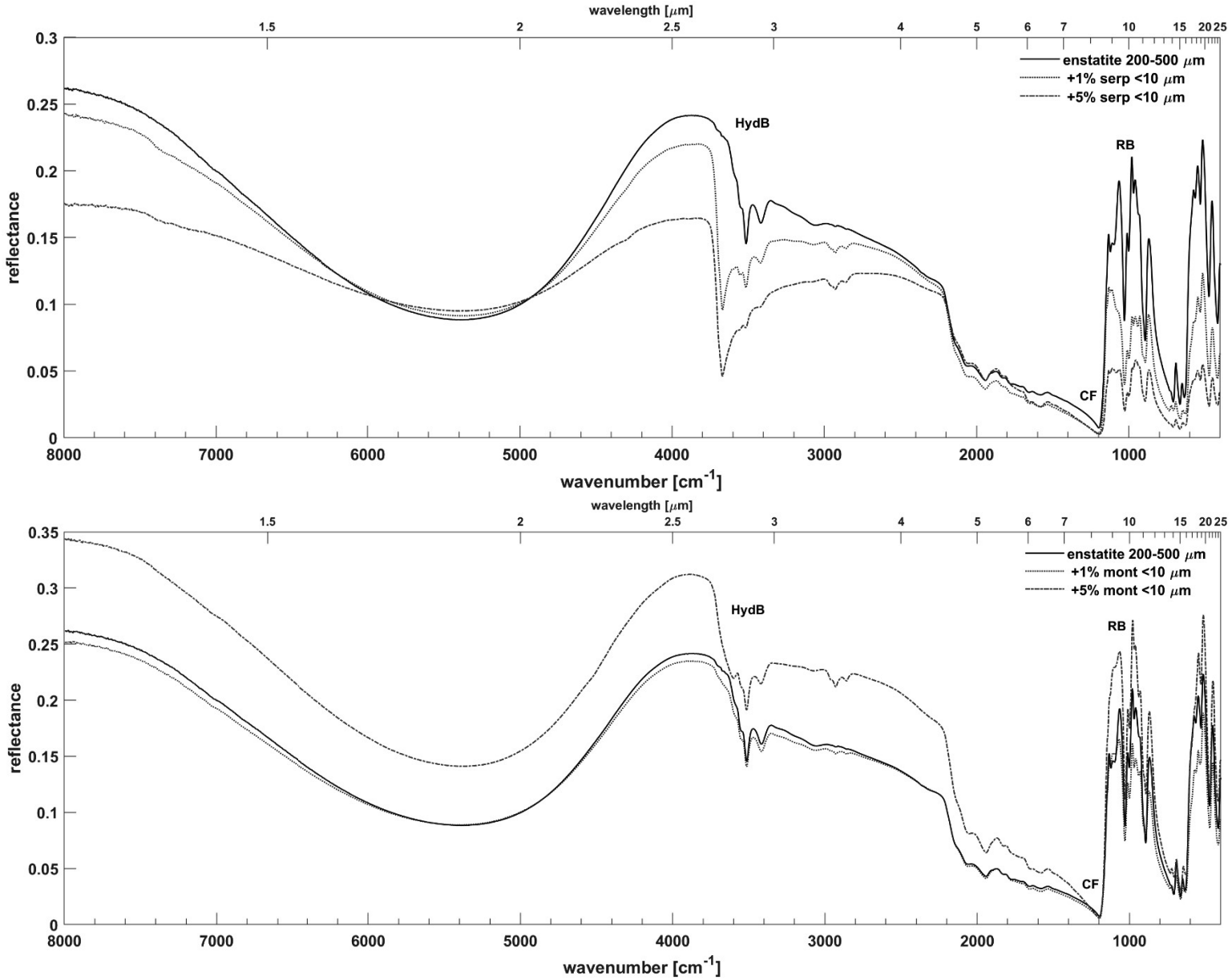

Figure 3 FTIR reflectance spectrum for enstatite with grain size 200-500 μm (solid line) compared to mixtures with serpentine (top) and montmorillonite (bottom) with < 10 μm grain size, at 1 wt % concentration (dotted blue line) and 5 wt% concentration (dash-dot red line). Position of the hydrated band (HydB), the Christiansen feature (CF) and the reststrahlen bands (RB) are highlighted on the spectrum.

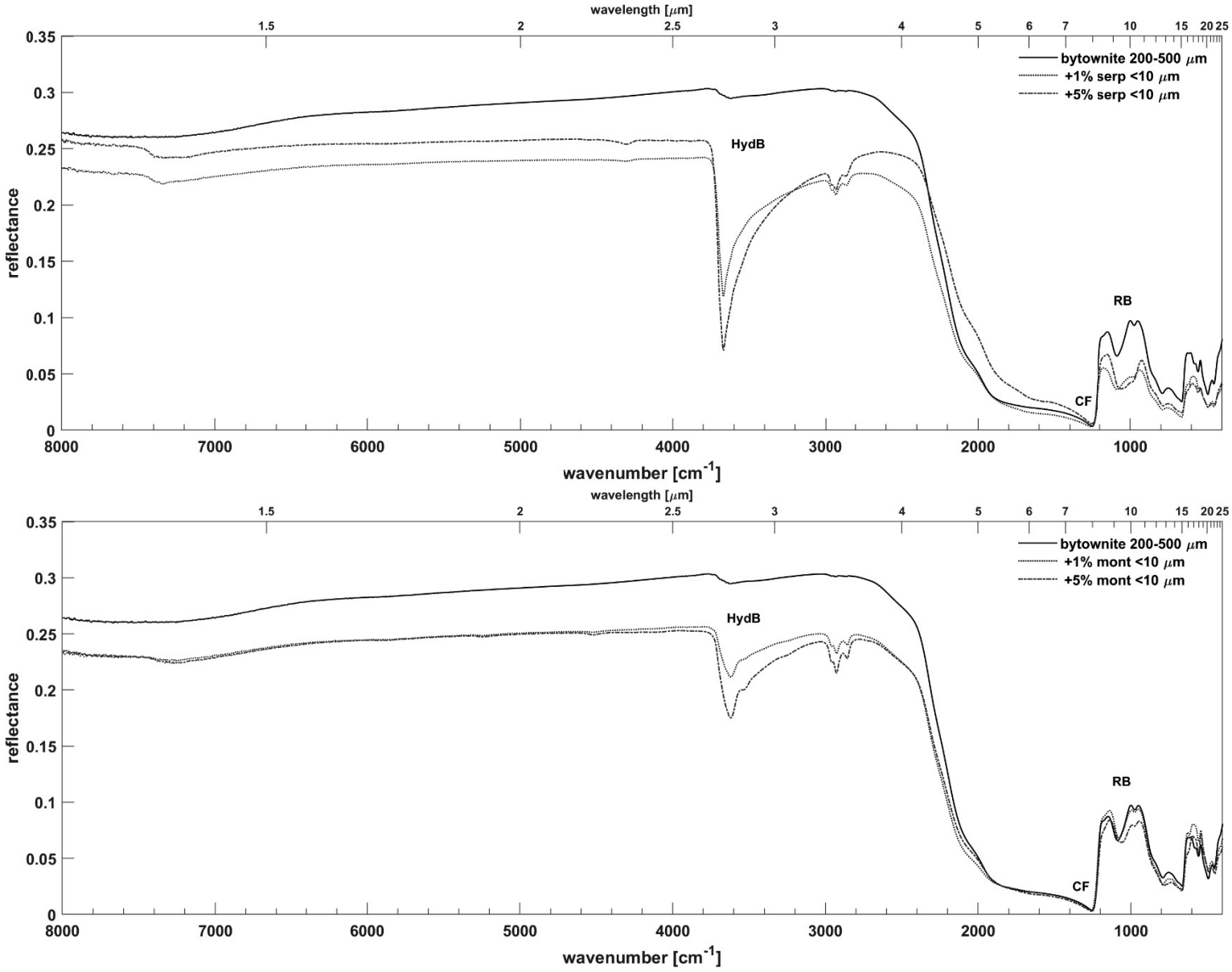

Figure 4 FTIR reflectance spectrum for bytownite with grain size 200-500 μm (solid line) compared to mixtures with serpentine (top) and montmorillonite (bottom) with < 10 μm grain size, at 1 wt % concentration (dotted blue line) and 5 wt% concentration (dash-dot red line). Position of the hydrated band (HydB), the Christiansen feature (CF) and the reststrahlen bands (RB) are highlighted on the spectrum.

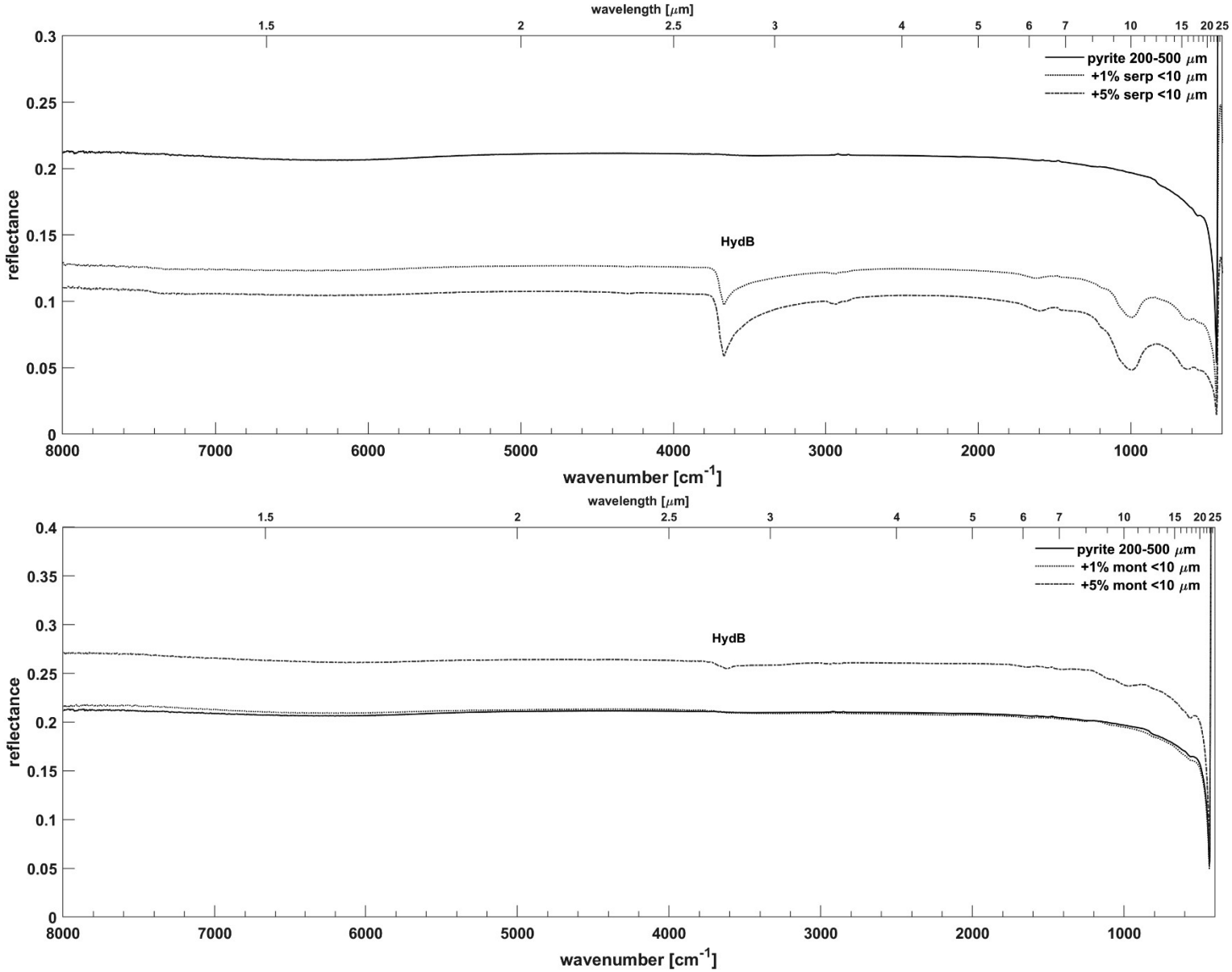

Figure 5 FTIR reflectance spectrum for pyrite with grain size 200-500 μm (solid line) compared to mixtures with serpentine (top) and montmorillonite (bottom) with < 10 μm grain size, at 1 wt % concentration (dotted blue line) and 5 wt% concentration (dash-dot red line). Position of the hydrated band (HydB) is highlighted on the spectrum.

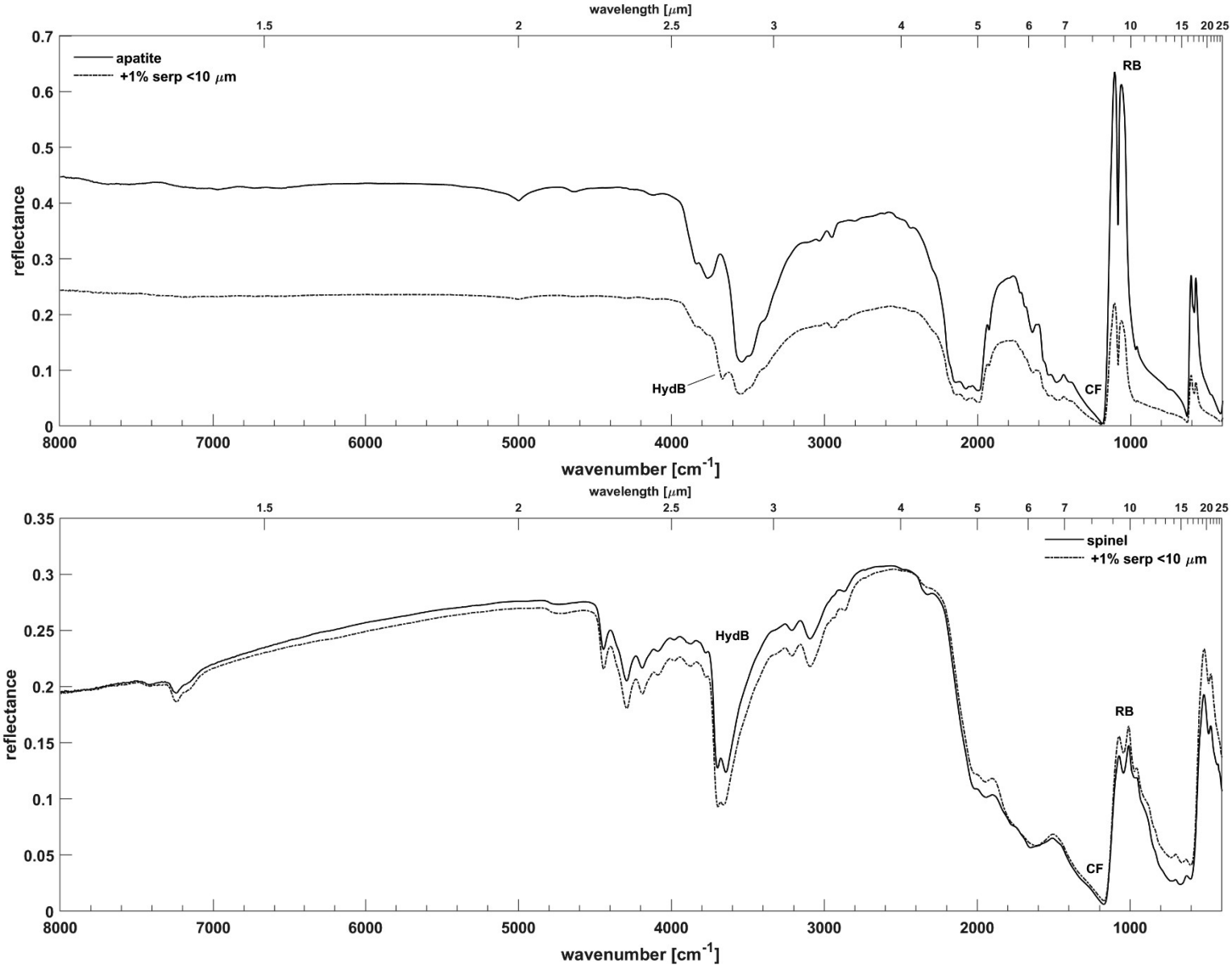

Figure 6 FTIR reflectance spectrum for apatite (top) and spinel (bottom) with grain size 200-500 µm (solid line) compared to mixtures with serpentine with < 10 µm grain size, at 1 wt % concentration (dotted blue line). Position of the hydrated band (HydB), the Christiansen feature (CF) and the reststrahlen bands (RB) are highlighted on the spectrum.

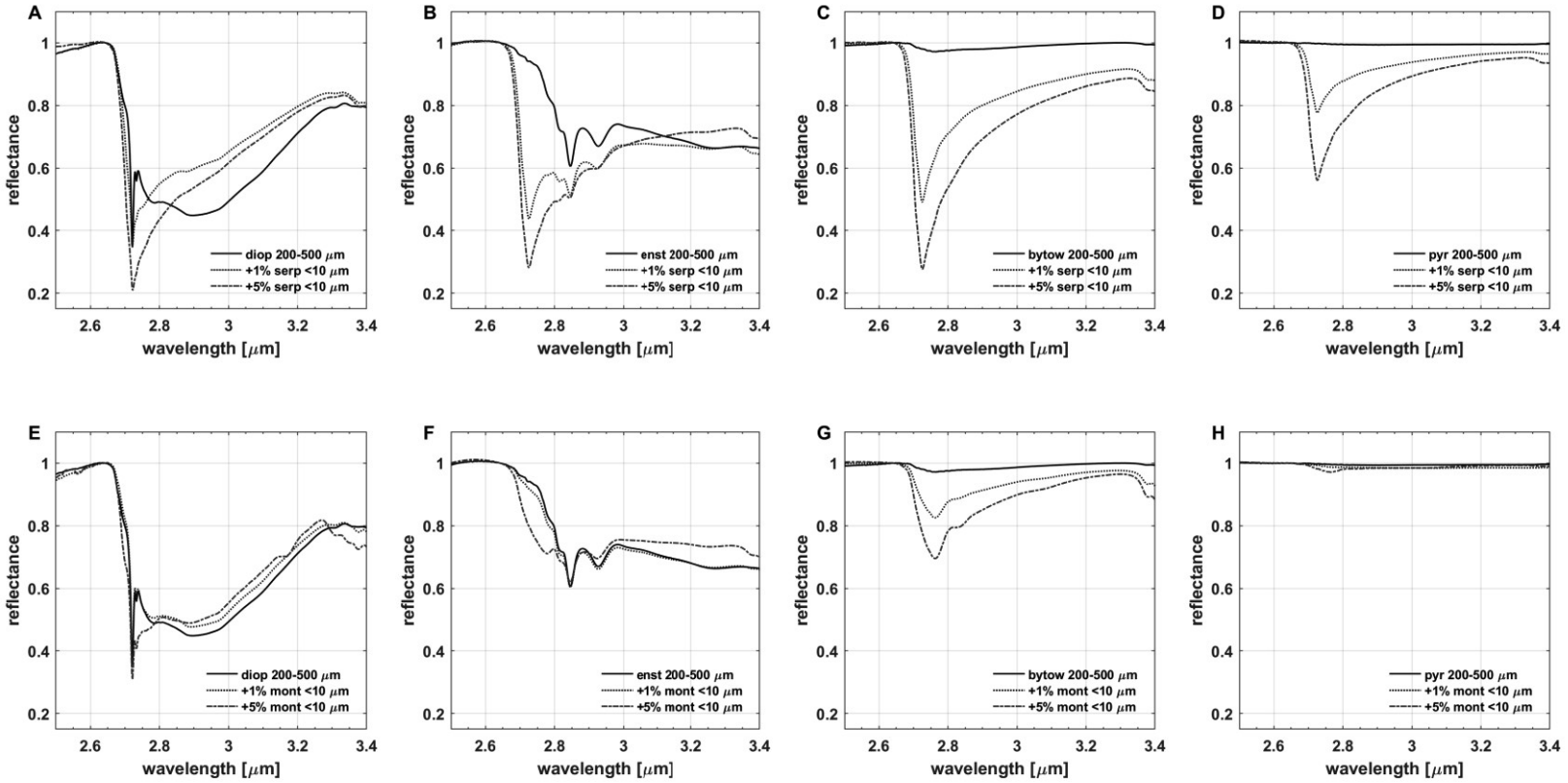

Figure 7 Detail of hydrated band around 2.7 μm for hydrated minerals serpentine (top panels) and montmorillonite (bottom panels) with grain size < 10 μm mixed at 1 wt% (dotted blue line) and 5 wt% concentration (dash-dot red line) with: pyroxene diopside (panels A and E), pyroxene enstatite (panel B and F), plagioclase bytownite (panel C and G) and iron sulfide pyrite (panel D and H).

4. Discussion and Conclusions

4.1 Results discussion

As visible in Figures 2-6, the presence of a hyperfine hydrate component in a much smaller amount (1 wt% and 5 wt%) than an anhydrous coarse component can change the infrared spectrum in both the NIR and MIR. These changes are more evident in the NIR region where the bands related to the presence of OH in the structure of hydrated minerals are present. A summary of the changes occurring in the infrared spectrum of the mixtures compared to the pure anhydrous mineral is reported in Table 4.

With only 1 wt% hyperfine hydrate material, depending on the anhydrous mineral used as the base for the mixture, some of the OH stretching overtone bands (e.g. 2.3 μm) can be distinctly observed. Of course, the most obvious change concerns the OH stretching band (around 2.7 μm). Whether the base mineral has a native band due to OH/H_2O defects in the structure or it is completely anhydrous, a definite change in the band shape occurs. Among the two hyperfine hydrated minerals analyzed, serpentine and montmorillonite, the former is more effective in altering the band at 2.7 μm, especially in the presence of OH defects in the anhydrous mineral (Figure 7).

In the case of pyroxenes, prominent features in the NIR region may appear due to ferrous iron absorption and crystal field effects. Usually, a feature at 1 μm is present, while one at 2 μm may not be visible. This depends on crystallographic site occupancy of the iron called M1 and M2 sites (Burns 1970, Cloutis 2002). In the case of enstatite (Figure 3), the 2 μm band due to M2 site occupancy is distinctly dominant in the NIR spectrum and is not altered in its shape by the presence of the hydrated component, which may, however, reduces its spectral contrast. Diopside and bytownite (Figures 1 and 3, respectively), not manifesting a deep 2 μm band, are much more affected by the presence of hydrated minerals, although we should note that the diopside used in this work is Ca-rich and does not show a big 2 μm feature.

Changes in the MIR region are significantly less intense than in the NIR region. In almost all spectra, the major changes concern the decrease (or increase) in intensity with often some differences in the relative intensities of the various peaks. Christiansen features seems to not vary significantly between the single anhydrous mineral and the mixture of the same with hydrated hyperfine grains.

The "cross-over" bands region of anhydrous minerals between 2200 cm^{-1} (4.5 μm) and 1200 cm^{-1} (8.3 μm) is usually less affected by the mixing with the hyperfine hydrated component; thus not being affected by possible contamination of other minerals, this region can certainly be taken as a reference for determining the anhydrous component (Kremer et al 2020), although not representative of the actual mineralogy of the whole sample.

The addition of hydrated minerals in several samples leads to the appearance of small peaks in the region around 750/700 µm. This is found for example in diopside mixed with montmorillonite or enstatite mixed with serpentine and montmorillonite. Remarkably, this peak appearing in the spectrum of the mixture and unrelated to the anhydrous mineral seems to be connected with minor features in the hydrated mineral spectrum as shown in Supplementary Material Figure S1, bottom right panel.

It may be of interest to think about the potential effects that would be observed in the case of contamination of hydrated minerals with grain sizes larger than hyperfines. Of course with increasing grain size we can assume a decrease in the adhesion efficiency of hydrated grains on large anhydrous grains maintained mainly by interactions such as electrostatic attraction and Van der Waals forces. We can also expect a decrease in the homogeneity of the mix (prepared in weight percentages) with larger but fewer hydrated grains in the mix that may lead to difference in the IR spectrum between the samples.

It is also necessary to mention that not all pairings between nominally anhydrous and hydrous minerals analyzed in this work, reproduce typical alteration mineralogies. For example, serpentinization occurs on olivines and pyroxenes and not on feldspars, which on the contrary are preferential sites for the formation of clay minerals. Nonetheless, the coexistence of these minerals is characteristic in most mafic rocks and this type of association can be expected on a regolith composed of these rocks. We are however forcing certain pairing to put more emphasis on features to look for in the IR spectra of mixtures not only dependent on plausible geologic origin but also on hyperfine dust contamination that can be obtained on planetary rock surfaces: either contamination due to wind transport in bodies with an atmosphere or due to dust movement induced by meteoric bombardment or thermal cracking, as might occur on an asteroid.

4.2 Future application and conclusion

As presented in the introduction several planetary mission can benefit from these results. For example, the interpretation of infrared observations by Mars rovers should take into account these results, especially when rovers explore environments where the presence of hydrated minerals may be limited to certain areas such as the river delta of Jezero crater currently being explored by the Mars 2020 Perseverance rover (Farley et al 2022) with onboard an infrared spectrometer included in SuperCam suite (Fouchet et al 2022). The dispersion of fine or hyperfine hydrated component can be responsible for some of the discrepancy between orbital data, where the crater floor of Jezero appears poorly hydrated, and rocks of the crater floor where Perseverance found an almost ubiquitous hydrated features (Mandon et al 2022). Olivine-carbonate deposit with large grain size (> 500 µm) were already observed on Mars (Brown et al. 2020), therefore aeolian erosion and the subsequent re-deposition of hydrated

554 material on anhydrous ore formations can be misinterpreted as a widespread presence of
555 hydrated minerals that may instead be concentrated in a limited area. Moreover our results
556 are in agreement with previous laboratory data of mixture between bigger grain size anhydrous
557 mineral and small grain size hydrated minerals related to Mars (Mandon et al 2020).
558 Of course, the surfaces of asteroids and other small bodies may also be in a situation where
559 there is a mix of anhydrous and hydrated components. Although the presence of diffuse
560 hydrated material is expected based on the study of meteorites, its surprising homogeneity in
561 infrared observations (i.e. Hamilton et al 2019, Praet et al 2021) may be due to a scattering
562 effect of hyperfine particles in a fairly uniform layer over the entire surface. The samples
563 collected by these two missions will help us understand the nature of the observations made
564 from orbit.
565 Moreover, the nature of the composition of Phobos and Deimos, the two moons of Mars, that
566 will be studied by MMX mission will be able to benefit from these results. Indeed, it is still being
567 debated the origin and composition of the Martian moons, and a true faint feature at 2.7 μm
568 has been observed (with some uncertainty) on their surfaces. The laboratory data here
569 presented, combined with observations from the MIRS (Barucci et al 2021) spectrometer on
570 the spacecraft, will make it possible to unravel the nature of the composition of these two
571 objects.
572 As can be seen from our results, the addition of a hydrated component, which is minor in
573 percentage and has a much smaller grain size, can lead to very remarkable changes in the
574 NIR region especially in the hydrated band at 2.7 μm, while slightly affecting the MIR region.
575 The surface of many rocky bodies is covered with regolith, and these new laboratory data
576 show how even a small amount of hydrated mineral in the composition can influence the
577 overall final spectrum. Therefore, it is of paramount importance to have a very good
578 understanding of the spectroscopic changes induced by small variations in the mineral phases
579 for the correct interpretation of infrared data of planetary surfaces acquired by space missions,
580 both through remote sensing from orbit and on the ground by rover exploration. This work can
581 be the basis for a more in-depth and systematic study of the nature of infrared changes as a
582 consequence of the mixing of different minerals.
583
584
585

anhyd. min.	OH/H2O defects in base min	hyd. min.	mix%	modification of base mineral bands	modification of HydB	appearance of phyllosilicate minor bands
diopside	strong	serp.	1	negligible in pyx bands contrast	very strong	no
			5	moderate in pyx bands contrast	extremely strong	no
		mont.	1	null in pyx band contrast	very faint	no
			5	very faint in pyx band contrast	faint	very faint*
enstatite	moderate	serp.	1	slightly in pyx band contrast	strong	very faint
			5	moderate in pyx band contrast	very strong	faint
		mont.	1	negligible in pyx bands contrast	very faint	no
			5	moderate in pyx bands intensity	moderate	no
bytownite	negligible	serp.	1	slightly in pyx band contrast	extremely strong	very faint
			5	moderate in pyx band contrast	extremely strong	faint
		mont.	1	moderate in pyx band contrast	very strong	very faint
			5	moderate in pyx band contrast	very strong	very faint
pyrite	negligible	serp.	1	faint base mineral band	very strong	very faint
			5	faint base mineral band	very strong	very faint
		mont.	1	faint base mineral band	faint	no
			5	faint base mineral band	faint	no
spinel	strong	serp	1	negligible	faint	no
apatite	strong	serp	1	negligible	faint	no

* with an increase of base mineral OH defect bands

Table 4 Summary of spectroscopic modification in NIR wavelength region for each mixture sample.

5. Acknowledgement

G.P. and M. A. B. acknowledge support by Centre national d'études spatiales (CNES). J.R.B., T.F and M.A.C. acknowledge support from Italian Space Agency agreement 2017-48-H.0. L. M. was supported by a Texaco Postdoctoral prize fellowship awarded by the division of Geological and Planetary Sciences of Caltech. **The authors would like to thank the anonymous reviewers for their helpful comments that helped improve the text overall.**

6. Data Availability

The infrared and SEM data showed in this article will be shared on reasonable request to the corresponding author.

7. References

Adams J. B. and Goullaud L. H. (1978). Plagioclase feldspars - Visible and near infrared diffuse reflectance spectra as applied to remote sensing. Proceedings, 9th Lunar and Planetary Science Conference. pp. 2901–2909.

Agee, C. B., Wilson, N. V., McCubbin, F. M., et al. (2013). Unique meteorite from early amazonian Mars: water-rich basaltic breccia Northwest Africa 7034. Science, 339, 780–785, doi:10.1126/science.1228858

Bach, W., Paulick, H., Garrido, C. J., et al. (2006). Unraveling the sequence of serpentinization reactions: petrography, mineral chemistry, and petrophysics of serpentinites from MAR 15°N (ODP Leg 209, Site 1274). Geophys. Res. Lett., 33, L13306, doi:10.1029/2006GL025681

Barucci, M.A. et al. (2019). Multivariable statistical analysis of spectrophotometry and spectra of (162173) Ryugu as observed by JAXA Hayabusa2 mission. Astronomy & Astrophysics, 629, A13, doi:10.1051/0004-6361/201935851

Barucci, M. A., Reess, J.-M., Bernardi, P. et al. (2021). MIRS: an imaging spectrometer for the MMX mission. Earth Planets Space 73, 211, doi:10.1186/s40623-021-01423-2

Bibring J. P. et al. (2004). in Wilson A., Chicarro A., eds, ESA Special Publ. Vol. 1240, Mars Express: the Scientific Payload. ESA Publications Division, Noordwijk, Netherlands, p. 37

Bowey, J. E., and Hofmeister, A. M. (2005). Overtones of silicate and aluminate minerals and the 5–8 μm ice bands of deeply embedded objects. Monthly Notices of the Royal Astronomical Society, 358, 1383–1393, doi:10.1111/j.1365- 2966.2005.08848.x

Bowey, J. E., Hofmeister, A. M. and Keppel, E. (2020). Infrared spectra of pyroxenes (crystalline chain silicates) at room temperature. Monthly Notices of the Royal Astronomical Society, 497, 3658–3673, doi:10.1093/mnras/staa2227

Braakman, R. (2013). Mapping metabolism onto the prebiotic organic chemistry of hydrothermal vents. Proc Natl Acad Sci USA 110 (33) 13236-13237 doi:10.1073/pnas.131247011

Brown, A. J., Hook, S. J., Baldridge, A. M. et al. (2010). Hydrothermal formation of Clay-Carbonate alteration assemblages in the Nili Fossae region of Mars. Earth and Planetary Science Letters, 297 (1–2), 174-182, doi: 10.1016/j.epsl.2010.06.018

Brown, A. J. (2014). Spectral bluing induced by small particles under the Mie and Rayleigh regimes. Icarus, 239, 85-95, doi: 10.1016/j.icarus.2014.05.042

Brown, A. J., Viviano, C. E., Goudge, T. A. (2020). Olivine-Carbonate Mineralogy of the Jezero Crater Region. J. Geophys. Res. Planet, 125 (3), e2019JE006011, doi: 10.1029/2019JE006011

Burns, R.G. (1970). Site preferences of transition metal ions in silicate crystal structures. Chemical Geology, 5, 4, 275-283 doi:10.1016/0009-2541(70)90045-8

Clark, R. N., King, T. V. V., Klejwa, M., et al. (1990). High spectral resolution reflectance spectroscopy of minerals. J. Geophys. Res. Solid Planet, 95 (B8), 12653-12680, doi:10.1029/JB095iB08p12653

Clark III, B. C., Arvidson, R. E., Gellert, R. et al. (2007). Evidence for montmorillonite or its compositional equivalent in Columbia Hills, Mars. J. Geophys. Res., 112, E06S01, doi:10.1029/2006JE002756

Carter, J., Loizeau, D., Mangold, N., et al. (2013). Widespread surface weathering on early Mars: A case for a warmer and wetter climate. Icarus, 248, 373-382, doi:10.1016/j.icarus.2014.11.011

Christensen, P. R. ; Mehall, G. L. ; Silverman, S. H. ; Anwar, S.; Cannon, G.; Gorelick, N.; Kheen, R.; Tourville, T. et al. (2003). Miniature Thermal Emission Spectrometer for the Mars Exploration Rovers. Journal of Geophysical Research, 108, E12, id. 8064 doi: 10.1029/2003JE002117

Changela, H. G., Chatzitheodoridis, E., Antunes, A. et al. 2022. Mars: new insights and unresolved questions - Corrigendum. International Journal of Astrobiology, 21 (1), pp. 46 doi: 10.1017/S1473550421000380

Chu, P.M., Guenther, F.R., Rhoderick, G.C. and Lafferty, W.J. (1999). The NIST Quantitative Infrared Database, J. Res. Natl. Inst. Stand. Technol., 104, 59 doi:10.6028/jres.104.004

Cloutis, E. A. (2002). Pyroxene reflectance spectra: Minor absorption bands and effects of elemental substitutions. Journal of Geophysical Research: Planets. 107, E6 6-1-6-12, doi:10.1029/2001JE001590

679 Cloutis, E. A., Hudon, P., Hiroi, T. et al. (2011). Spectral reflectance properties of
680 carbonaceous chondrites: 2. CM chondrites. Icarus, 216, 1, 309-346
681 doi:10.1016/j.icarus.2011.09.009
682
683 **Conel, J. E. (1969) Infrared emissivities of silicates: Experimental results and a cloudy**
684 **atmosphere model of Spectral emission from condensed particulate mediums.**
685 **Journal of Geophysical Research, 74 (6), 1614-1634 doi: 10.1029/JB074i006p01614**
686
687 DeMeo, F. E., Alexander, C. M. O'D., Walsh, K. J., Chapman, C. R., Binzel, R. P. (2015).
688 The Compositional Structure of the Asteroid Belt. In Michel, P., DeMeo, F. E. Bottke, W. F.
689 *Asteroid IV*, University of Arizona Press, Tucson.
690
691 Dodd, R. T., (1981). Meteorites: A Chemical-Petrologic Synthesis, Cambridge Univ. Press,
692 New York, ISBN:978-0521295574
693
694 **Domagal-Goldman S. D. and Wright K. E. (Ed.) 2016. The Astrobiology Primer v2.0.**
695 **Astrobiology, vol. 16, issue 8, pp. 561-653 doi: 10.1089/ast.2015.1460**
696
697 Ehlmann, B. L., Mustard, J. F., Clark, R. N., et al. (2011). Evidence for low-grade
698 metamorphism, hydrothermal alteration, and diagenesis on Mars from phyllosilicate mineral
699 assemblages. Clays Clay Mineral, 59, 359–377, doi:10.1346/CCMN.2011.0590402
700
701 Ehlmann, B. L., Mustard, J. F., and Murchie, S. L. (2010). Geologic setting of serpentine
702 deposit on Mars. Geophys. Res. Lett., 37, L0620, doi:10.1029/2010GL042596
703
704 Ehlmann, B. L., Mustard, J. F., Swayze, G. A., et al. (2009). Identification of hydrated silicate
705 minerals on Mars using MRO-CRISM: geologic context near Nili Fossae and implications for
706 aqueous alteration. J. Geophys. Res., 114, E00D08, doi:10.1029/2009JE003339
707
708 **Farkas-Takács, A., Kiss, C., Góbi, S. and Kereszturi, Á (2022). Serpentinization in the**
709 **Thermal Evolution of Icy Kuiper Belt Objects in the Early Solar System. Planet. Sci. J.,**
710 **3, 54 doi: 10.3847/PSJ/ac5175**
711
712 Farley, K. A.; Williford, K. H.; Stack, K. M.; Bhartia, R.; Chen, A.; de la Torre, M.; Hand, K.;
713 Goreva, Y. et al 2020. Mars 2020 Mission Overview. Space Science Reviews, 216, 8, id.142
714 doi: 10.1007/s11214-020-00762-y
715
716 **Fornaro, T., Boosman, A., Brucato, J. R. et al. (2018). UV irradiation of biomarkers**
717 **adsorbed on minerals under Martian-like conditions: Hints for life detection on Mars.**
718 **Icarus, 313, 38-60 doi: 10.1016/j.icarus.2018.05.001**
719
720 Fouchet, T.; Reess, J.-M.; Montmessin, F.; Hassen-Khodja, R.; Nguyen-Tuong, N.; Humeau,
721 O. et al. (2022). The SuperCam infrared spectrometer for the perseverance rover of the
722 Mars2020 mission. Icarus, 373, id. 114773, doi: 10.1016/j.icarus.2021.114773
723
724 Gaffey, M.J. (1986). The spectral and physical properties of metal in meteorite assemblages:
725 Implications for asteroid surface materials. Icarus, 66, 3, 468-486 doi: 10.1016/0019-
726 1035(86)90086-2

Hamilton, V.E., Simon, A.A., Christensen, P.R. et al. (2019). Evidence for widespread hydrated minerals on asteroid (101955) Bennu. Nat Astron 3, 332–340 doi:10.1038/s41550-019-0722-2

Haggerty, S. E. (2016). Spinel in planetary system. American Mineralogist, 101 (1), 5–6, doi:10.2138/am-2016-5554

Horgan, B. H. N., Cloutis, E. A., Mann, P. et al. (2014). Near-infrared spectra of ferrous mineral mixtures and methods for their identification in planetary surface spectra. Icarus, 234, 132-154, doi:10.1016/j.icarus.2014.02.031

Huguenin, R. L. (1987). The silicate component of Martian dust, Icarus, 70, 162–188, doi:10.1016/0019-1035(87)90083-2

Hu, S., Lin, Y., Zhang, J., Hao, J., Feng, L., Xu, L., Yang, W., Yang, J. (2014). NanoSIMS analyses of apatite and melt inclusions in the GRV 020090 Martian meteorite: Hydrogen isotope evidence for recent past underground hydrothermal activity on Mars. Geochimica et Cosmochimica Acta, 140, 321-333, doi: 10.1016/j.gca.2014.05.008

Iiishi, K., Tomisaka, T, Katô, T., et al. (1971a). Isomorphous substitution and infrared and far infrared spectra of the feldspar group. Neues Jb. Mineral. Abh., 115 (1), 98-119.

Iiishi, K., Tomisaka, T, Katô, T., et al. (1971b). The force field of K feldspar. Z Kristallogn, 134, 213-229, doi: 10.1524/zkri.1971.134.3-4.213

Johnson, J. R. et al 2002. Dust coatings on basaltic rocks and implications for thermal infrared spectroscopy of Mars. Journal of Geophysical Research: Planets, 107, E6, 2.1-2.19, doi: 10.1029/2000JE001405

Kiddel, C. B. et al. (2018). Spectral Reflectance of Powder Coatings on Carbonaceous Chondrite Slabs: Implications for Asteroid Regolith Observations. Journal of Geophysical Research: Planets, 123, doi: 10.1029/2018JE005600

Kitazato, K., Iwata, T., Abe, M., et al. (2019). The surface composition of asteroid 162173 Ryugu from Hayabusa2 near-infrared spectroscopy. Science, 364, 6437, 272-275 doi:10.1126/science.aav7432

Kremer, C. H., Mustard,J. F. and Pieters, C. M. (2020). Cross-Over Infrared Spectroscopy: A New Tool for the Remote Determination of Olivine Composition. Geophysical Research Letters, 47, 20, e2020GL089151, doi:10.1029/2020GL089151

Kuramoto K. et al. (2022). Martian moons exploration MMX: sample return mission to Phobos elucidating formation processes of habitable planets. Earth Planets Space, 74, 12 doi:10.1186/s40623-021-01545-7

Mandon, L., Beck, P., Quantin-Nataf, C. et al. (2020). ROMA: A Database of Rock Reflectance Spectra for Martian In Situ Exploration. Earth and Space Science, 9 (1), e2021EA001871, doi: 10.1029/2021EA001871

Mandon, L., Quantin-Nataf, C., Royer, C. et al. (2022). Reflectance of Jezero crater floor: 2. Mineralogical interpretation. Journal of Geophysical Research: Planets, e2022JE007450 (accepted) doi: 10.1029/2022JE007450

Mason, B. (1968). Pyroxenes in meteorites. Lithos, 1 (1), 1-11, doi:10.1016/S0024-4937(68)80030-1

Maurette, M., Duprat, J., Engrand, C., et al. (2000). Accretion of neon, organics, CO2, nitrogen and water from large interplanetary dust particles on the early Earth. Planetary and Space Science, 48 (11) , 1117-1137 doi: 10.1016/S0032-0633(00)00086-6

McCubbin, F. M., Boyce, J. W., Srinivasan, P., Santos, A. R., Elardo, S. M. et al. 2016. Heterogeneous distribution of H2O in the Martian interior: Implications for the abundance of H2O in depleted and enriched mantle sources. Meteoritics & Planetary Science, 51 (11) 2036-2060, doi: 10.1111/maps.12639

Michel, P., Küppers, M., Campo Bagatin, A. et al. (2022). The ESA Hera Mission: Detailed Characterization of the DART Impact Outcome and of the Binary Asteroid (65803) Didymos. Planet. Sci. J. 3 160 doi: 10.3847/PSJ/ac6f52

Milam, K. A., McSween Jr., H. Y., Moersch, J., et al. (2010). Distribution and variation of plagioclase compositions on Mars. J. Geophys. Res. Planets, 115, E09004, doi:10.1029/2009JE003495

Moody, J. B. (1976). Serpentinization: a review. Lithos, 9, 2, 125-138 doi: 10.1016/0024-4937(76)90030-X

Morbidelli, A., Chambers, J., Lunine, J. I., et al. (2000). Source regions and time scales for the delivery of water to Earth. Meteoritics & Planetary Science, 35, 6, 1309-1320 doi:10.1111/j.1945-5100.2000.tb01518.x

Moskovitz, N. A., Jedicke, R., Gaidos, E., et al. (2008). The distribution of basaltic asteroids in the Main Belt. Icarus, 198, 77-90, doi:10.1016/j.icarus.2008.07.006

Murchie S. et al. , 2007, J. Geophys. Res. (Planets), 112, E05S03 doi:10.1029/2006JE002682

Mustard, J. F. and Hays, J. E. (1997). Effects of Hyperfine Particles on Reflectance Spectra from 0.3 to 25 μm. Icarus, 125, 1, 145-163, doi: 10.1006/icar.1996.5583

Mustard, J. F., Poulet, F., Gendrin, A., et al. (2005). Olivine and Pyroxene Diversity in the Crust of Mars, Science, 307 (5715), 1594-1597, doi:10.1126/science.1109098

Mustard, J., Murchie, S., Pelkey, S. et al. (2008). Hydrated silicate minerals on Mars observed by the Mars Reconnaissance Orbiter CRISM instrument. Nature 454, 305–309 doi: 10.1038/nature07097

Omori, K. (1921). Analysis of the Infrared Absorption Spectrum of Diopside. American Mineralogist, 56 (9-10), 1607-1616.

Praet, A., Barucci, M. A., Clark, B. E. et al. (2021). Hydrogen abundance estimation and distribution on (101955) Bennu. Icarus, 363, 114427 doi: 10.1016/j.icarus.2021.114427

Poggiali, G. Brucato, J. R., Dotto, E. et al. (2021). Temperature dependent mid-infrared (5–25 μm) reflectance spectroscopy of carbonaceous meteorites and minerals: Implication for remote sensing in Solar System exploration. Icarus, 354 (15), 114040 doi: 10.1016/j.icarus.2020.114040

Poggiali, G., Matsuoka, M., Barucci, M. A. et al. (2022). Phobos and Deimos surface composition: search for spectroscopic analogues. MNRAS, 516 (1), 465–476 doi:10.1093/mnras/stac2226

Pommerol, A. and Schmitt, B. (2008). Strength of the H2O near-infrared absorption bands in hydrated minerals: Effects of particle size and correlation with albedo. J. Geophys. Res., 113, E10009 doi:10.1029/2007JE003069, 2008

Rubin, A. and Ma, C. (2021). Meteorite Mineralogy. Cambridge Univ. Press, New York, doi: 10.1017/9781108613767

Salisbury, J.W. and L. Walter (1989). Thermal infrared (2.5-13.5 um) spectroscopic remote sensing of igneous rock types on particulate planetary surfaces. J. Geophys. Res., 94, 9192-9202, doi:10.1029/JB094iB07p09192

Salisbury, J.W., D'Aria, D. M. and Jarosewich, E. (1992). Midinfrared (2.5-13.5 μm) reflectance spectra of powdered stony meteorites. Icarus, 92, 280--297

Scott, E.R.D. (2020). Iron Meteorites: Composition, Age, and Origin. Oxford Research Encyclopedia of Planetary Science, Oxford University Press. doi: 10.1093/acrefore/9780190647926.013.206

Shock, E. and Canovas, P. (2010). The potential for abiotic organic synthesis and biosynthesis at seafloor hydrothermal systems. Geofluids 10, 161–192 doi:10.1111/j.1468-8123.2010.00277.x

Skulteti, A., Kereszturi, A., Szabo, M. et al. (2020). Mid-infrared spectroscopic investigation of meteorites and perspectives for thermal infrared observations at the binary asteroid Didymos. Planetary and Space Science, 184, 104855 doi: 10.1016/j.pss.2020.104855

Viviano-Beck, C. E., Seelos, F. P., Murchie, S. L., Kahn, E. G., Seelos, K. D., Taylor, H. W., et al. (2014). Revised CRISM spectral parameters and summary products based on the

currently detected mineral diversity on Mars. J. Geophys. Res. Planets, 119, 1403–1431, doi:10.1002/2014JE004627

Williford, K. H., Farley, K. A., Stack, K. M., Allwood, A. C., Beaty, D., Beegle, L. W., et al. (2018). "The NASA Mars 2020. rover mission and the search for extraterrestrial life," in: From Habitability to Life on Mars. eds N. Cabrol and E. Grim (Amsterdam: Elseivier), 275–308. doi: 10.1016/B978-0-12-809935-3.00010-4

Wu, S.; He, M.; Yang, M.; Zhang, B.; Wang, F.; Li, Q. (2021). Near-Infrared Spectroscopy Study of Serpentine Minerals and Assignment of the OH Group. Crystals, 11, 1130. doi:10.3390/cryst11091130

Yang, Y., Xia, Q. K., Feng, M. et al. (2012) OH in natural orthopyroxene: an in situ FTIR investigation at varying temperatures. Phys. Chem. Minerals, 39, 413–418, doi:10.1007/s00269-012-0496-x

Yu, Y., and Gee, J. (2005). Spinel in Martian meteorite SaU 008: implications for Martian magnetism. Earth Planet. Sci. Lett., 232, 287–294, doi: 10.1016/j.epsl.2004.12.015

Zolotov M.Y. and Shock E.L. (2005) Formation of jarosite-bearing deposits through aqueous oxidation of pyrite at Meridiani Planum, Mars. Geophys. Res. Lett., 32, L21203, doi:10.1029/2005GL024253

Supplementary material

	serp		mont		diop		enst		byto		pyr		apat		spinel	
	avg	σ	*avg*	σ	*avg*	σ	*avg*	σ	*avg*	σ	*avg*	σ	*avg*	σ	*avg*	σ
SiO_2	50,0	3,0	69,2	1,7	53,0	3,0	59,0	1,5	50,8	0,9	-	-	-	-	48,0	10,0
TiO_2	-	-	-	-	-	-	-	-	-	-	-	-	-	-	0,7	0,7
Al_2O_3	2,2	0,4	19,2	1,2	0,4	0,3	1,3	0,2	30,9	1,1	-	-	-	-	13,0	7,0
FeO*	10,0	2,0	2,0	1,1	1,3	0,5	6,2	0,6	0,4	0,1	-	-	-	-	6,0	2,0
MnO	-	-	-	-	0,3	0,2	0,1	0,2	-	-	-	-	-	-	-	-
MgO	37,4	1,6	6,1	0,3	16,5	1,7	32,8	1,7	0,3	0,1	-	-	-	-	26,0	9,0
CaO	-	-	3,3	0,6	28,0	2,0	0,6	0,1	13,7	1,1	-	-	60,7	0,9	-	-
Na_2O	-	-	-	-	0,1	0,1	0,1	0,1	3,8	0,5	-	-	-	-	-	-
K_2O	-	-	0,3	0,5	-	-	-	-	0,0	0,0	-	-	-	-	6,0	6,0
P_2O_5	-	-	-	-	-	-	-	-	-	-	-	-	38,7	0,8	-	-
Cl	-	-	-	-	-	-	-	-	-	-	-	-	0,7	0,1	-	-
Fe	-	-	-	-	-	-	-	-	-	-	51,0	4,0	-	-	-	-
S	-	-	-	-	-	-	-	-	-	-	49,0	4,0	-	-	-	-
Cr2O3	0,7	0,9	-	-	-	-	-	-	-	-	-	-	-	-	-	-
NiO	0,4	0,3	-	-	-	-	-	-	-	-	-	-	-	-	-	-

Table S1 Mineral samples composition measured using SEM-EDS (all oxides are in wt.%)

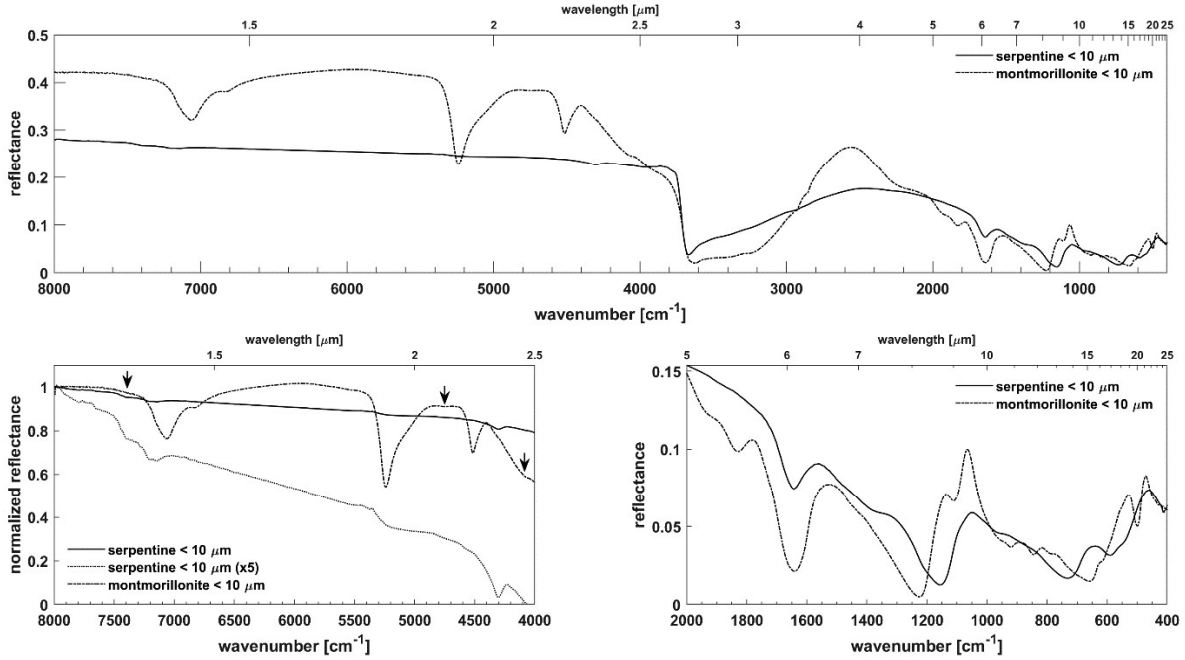

Figure S1 Infrared spectrum of serpentine (solid line) and montmorillonite (dash-dot line). Top panel, full range of acquisition. Bottom left panel, detail of normalized reflectance in the NIR region 8000-4000 cm^{-1} (1.25-2.5 μm) with serpentine spectrum shown in original and with x5 magnitude to enhance the presence of minor bands (dotted line). Black arrows are showing position of very faint features in montmorillonite spectrum. Bottom right panel, detail of MIR region 2000-400 cm^{-1} (5-25 μm).

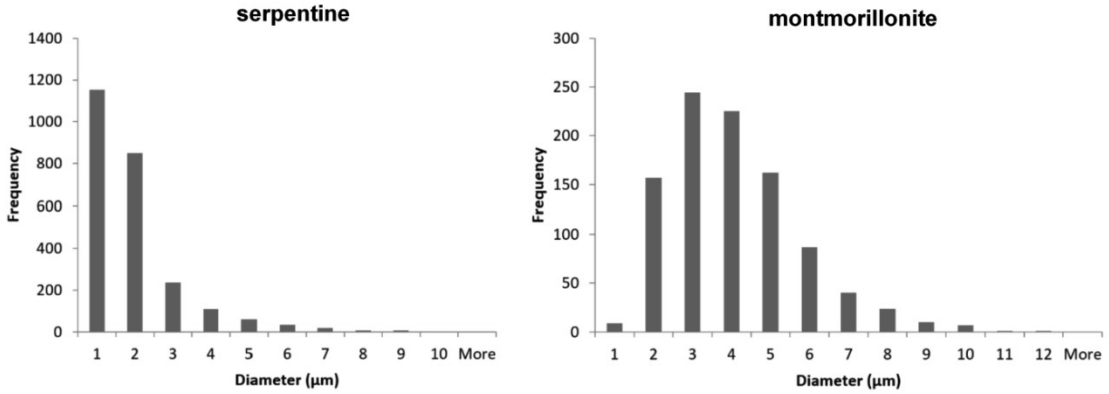

Figure S2 Grain size distribution in the serpentine sample (left) and montmorillonite sample (right) from SEM analysis

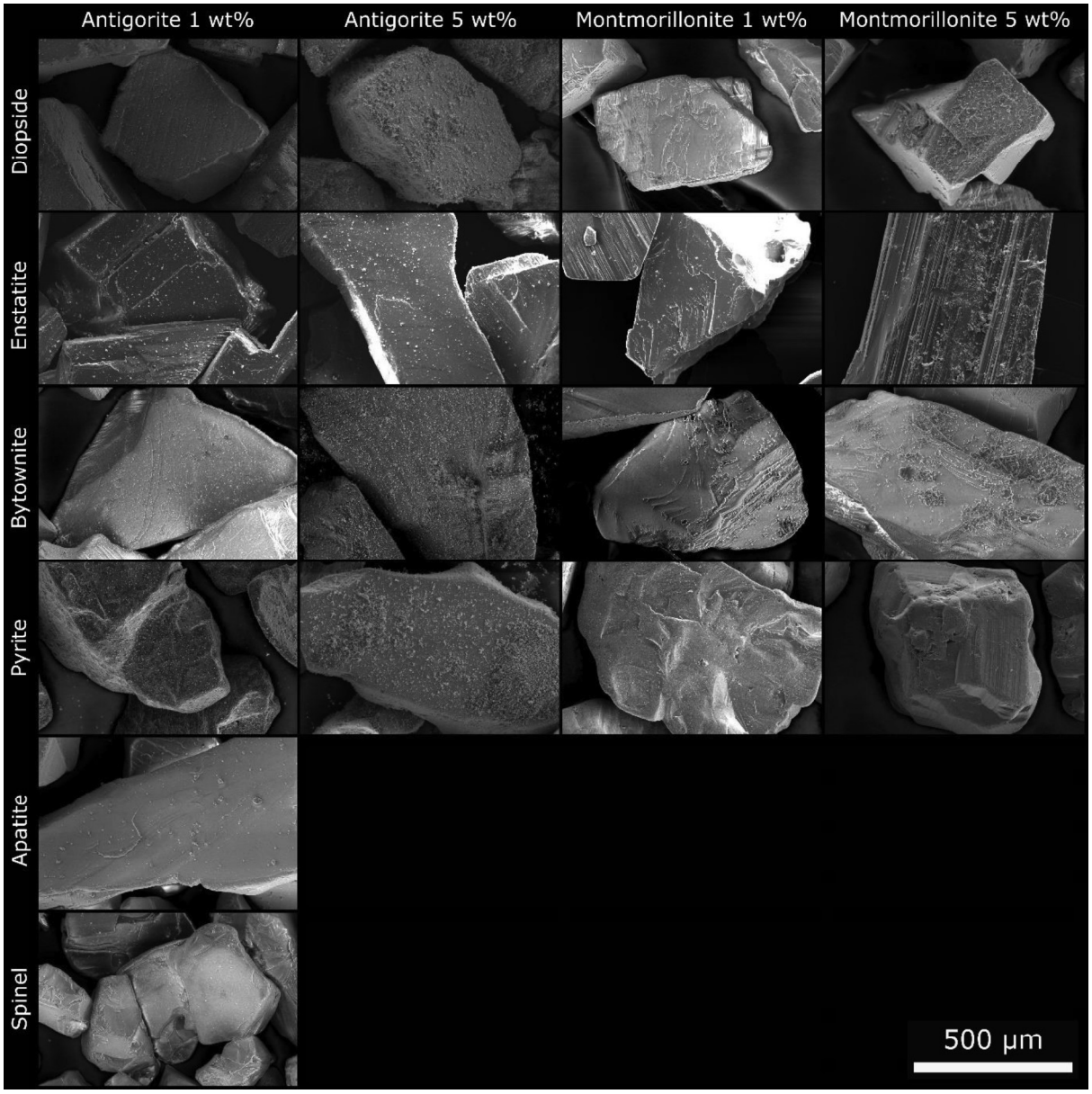

910

911 **Figure S3** Secondary electrons SEM image of all the mixtures prepared in this work. As visible in the
912 images the hyperfine hydrated component tends to stick on the flat surface of the bigger grain size
913 anhydrous component. Spinel and Antigorite were produced in just one combiantio due to shortage of
914 material. Scale is 500 µm for all the images.

915

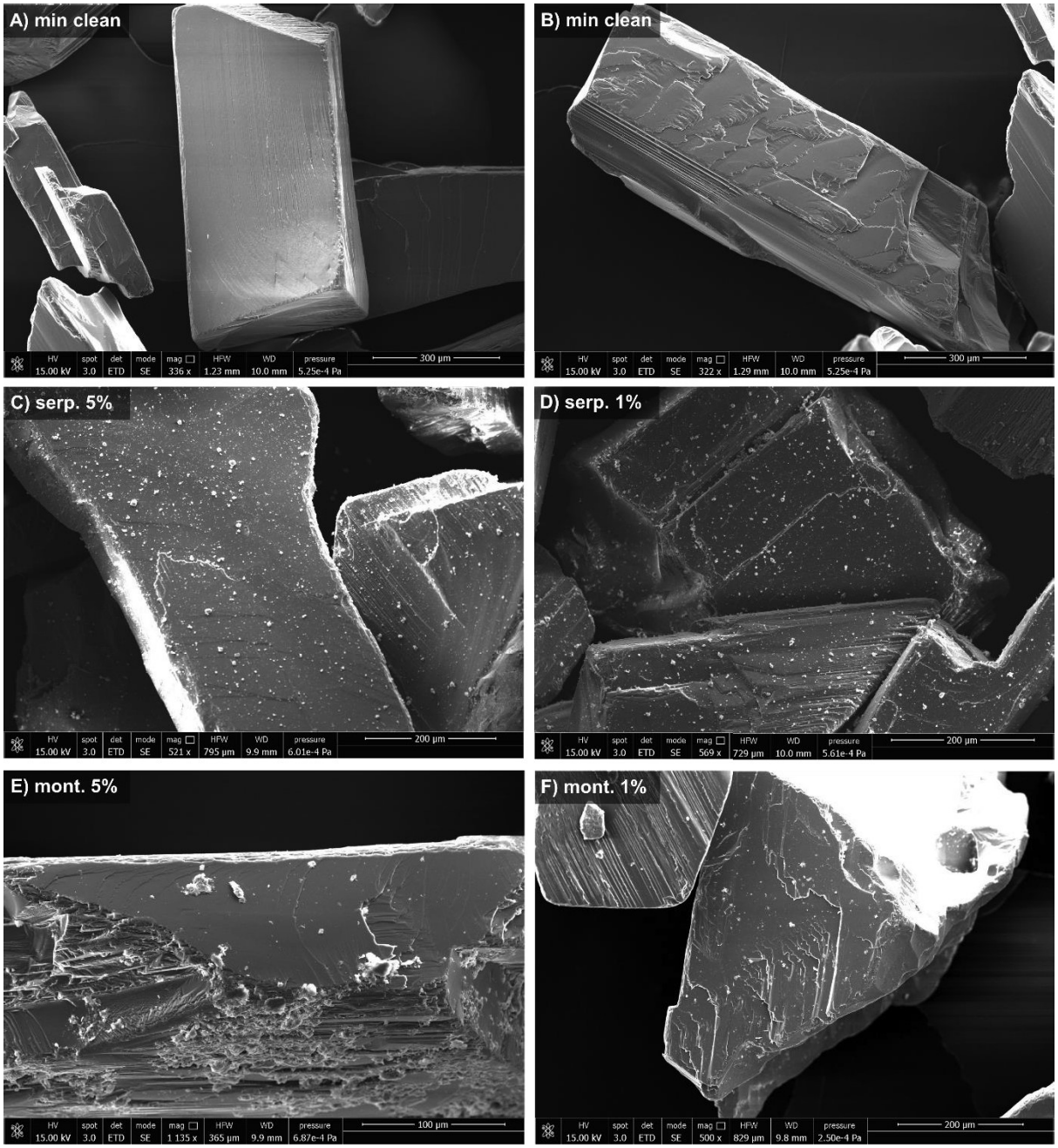

Figure S4 Secondary electrons SEM image of enstatite sample before (panel A and B) and after mixing with 5% and 1% of serpentine (panel C and D) and montmorillonite (panel E and F). As visible in the images of the mixed samples the hyperfine hydrated component tends to stick on the flat surface of the bigger grain size anhydrous component.